



LUND UNIVERSITY

Attosecond photoelectron interferometry: from wavepackets to density matrices

Laurell, Hugo

2023

[Link to publication](#)

Citation for published version (APA):

Laurell, H. (2023). *Attosecond photoelectron interferometry: from wavepackets to density matrices*. Atomic Physics, Department of Physics, Lund University.

Total number of authors:

1

General rights

Unless other specific re-use rights are stated the following general rights apply:

Copyright and moral rights for the publications made accessible in the public portal are retained by the authors and/or other copyright owners and it is a condition of accessing publications that users recognise and abide by the legal requirements associated with these rights.

- Users may download and print one copy of any publication from the public portal for the purpose of private study or research.
- You may not further distribute the material or use it for any profit-making activity or commercial gain
- You may freely distribute the URL identifying the publication in the public portal

Read more about Creative commons licenses: <https://creativecommons.org/licenses/>

Take down policy

If you believe that this document breaches copyright please contact us providing details, and we will remove access to the work immediately and investigate your claim.

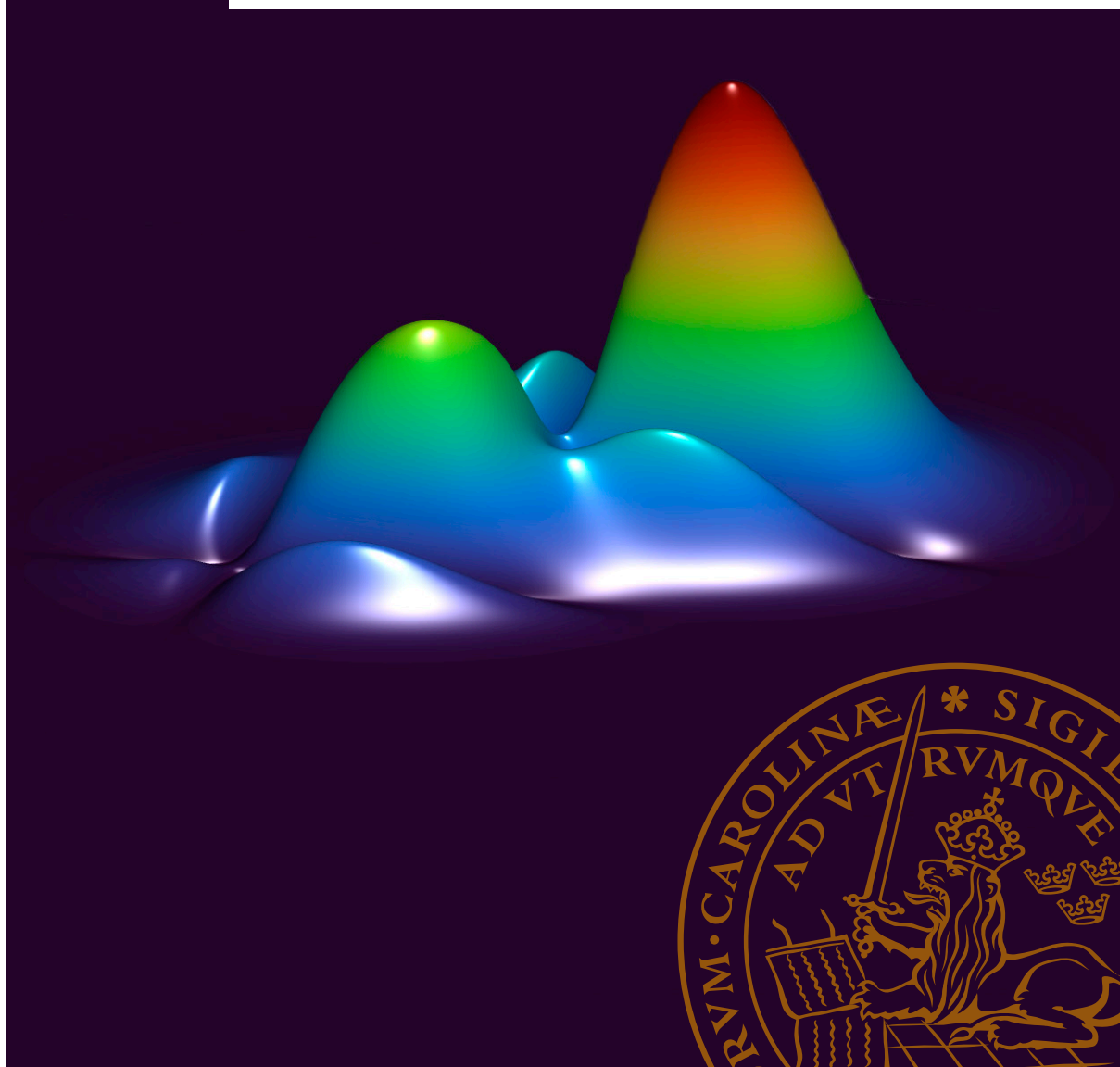
LUND UNIVERSITY

PO Box 117
221 00 Lund
+46 46-222 00 00

Attosecond photoelectron interferometry: from wavepackets to density matrices

HUGO LAURELL

ATOMIC PHYSICS | FACULTY OF ENGINEERING | LUND UNIVERSITY



Attosecond photoelectron interferometry: from wavepackets
to density matrices

Attosecond photoelectron interferometry: from wavepackets to density matrices

by Hugo Laurell



LUND
UNIVERSITY

Thesis for the degree of PhD in Physics

Thesis advisors: Prof. Anne L'Huillier, Dr. Cord L. Arnold,
Dr. Mathieu Gisselbrecht

Faculty opponent: Dr. Christian Ott

To be presented, with the permission of the Faculty of Engineering, LTH of Lund University,
for public criticism in Rydberg lecture hall at the Department of Physics on Friday, the 9th
of June 2023 at 09:15.

Organization LUND UNIVERSITY Atomic Physics Box 118 SE-221 00 LUND Sweden	Document name DOCTORAL DISSERTATION	
	Date of disputation 2023-06-09	
	Sponsoring organization	
Author(s) Hugo Laurell		
Title and subtitle Attosecond photoelectron interferometry: from wavepackets to density matrices		
<p>Abstract</p> <p>Through the advent of high-order harmonic generation and attosecond light pulses, photoionization dynamics has been studied on the attosecond time-scale, the intrinsic time-scale of such dynamics. When the electron leaves the atomic potential a phase shift is imprinted on the electron wavefunction. The measurement of this phase, together with amplitude allows us to determine the dynamics that of the photoionization.</p> <p>In this thesis, attosecond (10^{-18} s) and femtosecond (10^{-15} s) photoionization dynamics are studied using the photoelectron interferometry technique, Reconstruction of Attosecond Beating By Interference of two-photon Transitions (RABBIT). In RABBIT, the electron wavepacket is interfered with itself, and through this spectral interference, the spectral amplitude and phase can be retrieved.</p> <p>Attosecond time-delay measurements, are performed in argon and xenon where different aspects of electron correlation are investigated. In argon photoionization is studied in the region of the Cooper minimum, where the ionization cross section rapidly decrease. In xenon photoionization is studied across the $4d$ giant dipole resonance. Resonant dynamics is studied using energy-resolved RABBIT. The studied resonances are the $1s3p$, $1s4p$, $1s5p$ (below threshold) and $2s2p$ (above threshold) in He and $3s^{-1}4p$ (above threshold) in Ar. Most of the measurements in the thesis are angular-integrated.</p> <p>If the photoelectron is prepared as a mixed state, RABBIT is unsuccessful in characterizing the quantum state of the electron, since it cannot be represented as a wavefunction. Therefore a quantum state tomography protocol for photoelectrons (KRAKEN) was developed and tested experimentally in non-resonant ionization of helium, neon and argon. In the case of neon and argon, due to spin-orbit splitting, the entanglement between the photoelectron and ion leads to decoherence induced by incomplete measurements where the state of the ion is not measured.</p>		
Key words Quantum state tomography, Decoherence, Photoionization.		
Classification system and/or index terms (if any)		
Supplementary bibliographical information	Language English	
ISSN and key title 0281-2762	ISBN 978-91-8039-552-6 (print) 978-91-8039-553-3 (pdf)	
Recipient's notes	Number of pages 189	Price
	Security classification	

I, the undersigned, being the copyright owner of the abstract of the above-mentioned dissertation, hereby grant to all reference sources the permission to publish and disseminate the abstract of the above-mentioned dissertation.

Signature  _____

Date 2023-04-14

Attosecond photoelectron interferometry: from wavepackets to density matrices

by Hugo Laurell



LUND
UNIVERSITY

A doctoral thesis at a university in Sweden takes either the form of a single, cohesive research study (monograph) or a summary of research papers (compilation thesis), which the doctoral student has written alone or together with one or several other author(s).

In the latter case the thesis consists of two parts. An introductory text puts the research work into context and summarizes the main points of the papers. Then, the research publications themselves are reproduced, together with a description of the individual contributions of the authors. The research papers may either have been already published or are manuscripts at various stages (in press, submitted, or in draft).

Cover illustration front: Density matrix of the $3s^{-1}4p$ Fano resonance in argon.

Cover illustration back: Classical trajectories in the three-step model.

Funding information: The thesis work was financially supported by the Swedish Research Council, the European Research Council, infrastructure support by LTH, Crafoord Foundation, and the Knut and Alice Wallenberg Foundation.

pp. ii-83 © Hugo Laurell 2023

Paper I © 2021 The Authors under CC BY 4.0

Paper II © 2020 The Authors under CC BY 4.0

Paper III © 2022 The Authors under CC BY 4.0

Paper IV © The Authors

Paper V © 2022 The Authors under CC BY 4.0

Paper VI © 2022 The Authors under CC BY 4.0

Paper VII © The Authors

Paper VIII © The Authors

Faculty of Engineering, LTH, Atomic Physics

ISBN: 978-91-8039-552-6 (print)

ISBN: 978-91-8039-553-3 (pdf)

ISSN: 0281-2762

Printed in Sweden by Media-Tryck, Lund University, Lund 2023



Abstract

Through the advent of high-order harmonic generation and attosecond light pulses, photoionization dynamics has been studied on the attosecond time-scale, the intrinsic time-scale of such dynamics. When the electron leaves the atomic potential a phase shift is imprinted on the electron wavefunction. The measurement of this phase, together with amplitude allows us to determine the dynamics that of the photoionization.

In this thesis, attosecond (10^{-18} s) and femtosecond (10^{-15} s) photoionization dynamics are studied using the photoelectron interferometry technique, Reconstruction of Attosecond Beating By Interference of two-photon Transitions (RABBIT). In RABBIT, the electron wavepacket is interfered with itself, and through this spectral interference, the spectral amplitude and phase can be retrieved.

Attosecond time-delay measurements, are performed in argon and xenon where different aspects of electron correlation are investigated. In argon photoionization is studied in the region of the Cooper minimum, where the ionization cross section rapidly decrease. In xenon photoionization is studied across the $4d$ giant dipole resonance. Resonant dynamics is studied using energy-resolved RABBIT. The studied resonances are the $1s3p$, $1s4p$, $1s5p$ (below threshold) and $2s2p$ (above threshold) in He and $3s^{-1}4p$ (above threshold) in Ar. Most of the measurements in the thesis are angular-integrated.

If the photoelectron is prepared as a mixed state, RABBIT is unsuccessful in characterizing the quantum state of the electron, since it cannot be represented as a wavefunction. Therefore a quantum state tomography protocol for photoelectrons (KRAKEN) was developed and tested experimentally in non-resonant ionization of helium, neon and argon. In the case of neon and argon, due to spin-orbit splitting, the entanglement between the photoelectron and ion leads to decoherence induced by incomplete measurements where the state of the ion is not measured.

Popular Science Summary

The interaction of matter with light is along with gravity one of the two forces of nature that humans can directly experience. When the sun shines on our skin we can feel the heat from light being absorbed, in the receptors of our eyes light-matter interaction enables our vision. The dynamics of this interaction is ultimately due to by the interaction between electrons and photons, the quanta of light. The dynamics of the electron-photon interaction occur on the attosecond (10^{-18} s) time scale, where the proportion of 1 attosecond to 1 second is the same proportion as 1 second to the age of the universe. To uncover on how photons and electrons interact, it should be measured on these very short times.

In 1987, a new type of extreme ultraviolet laser was invented, with pulses of duration on the order of attoseconds. These laser pulses can be used as a very fast camera flash, to record a slow motion movie of how the electrons move. From this slow motion movie it is possible to learn how light interacts with matter.

When an atom absorbs a photon of sufficiently high energy, an electron can be removed from the atom. This effect is called the photoelectric effect. In this thesis, I have used such an attosecond laser to measure the dynamics of the photoelectric effect in different elements.

Quantum mechanics is the theory that describes how matter interacts with light. In quantum mechanics objects can have strange properties that seem unintuitive to everyday experience. For example, quantum objects can be in two places at once, a property called superposition. Additionally quantum objects can be entangled, what Einstein called, a spooky action at a distance. If two objects, A and B, are entangled an observation on A will change the state of B instantaneously, even if they are separated by a large distance. In this thesis, a method to measure the quantum state of a photoelectron is presented. Such measurements allow to characterize the quantum properties of the electron and may unravel how the the entanglement evolves between the electron and the atom under these very short time-scales.

One can argue that the work of this thesis is of little practical use. However basic research have repeatedly shown an ability to provide unexpected practical applications.

Populärvetenskaplig sammanfattning

Interaktionen mellan materia och ljus är tillsammans med gravitationen en av de två naturkrafter som människor direkt kan uppleva. När solen skiner på vår hud kan vi känna värmen från ljus som absorberas, i receptorerna i våra ögon möjliggör ljus-materia växelverkan vår syn. Dynamiken i denna interaktion beror ytterst på interaktionen mellan elektroner och fotoner. Dynamiken i ljus materia växelverkan sker på attosekundtidsskalan (10^{-18} s), där proportionen mellan 1 attosekund och 1 sekund är samma proportion som mellan 1 sekund och universums ålder. För att förstå hur fotoner och elektroner interagerar måste interaktionen mätas på dessa mycket korta tider.

1987 uppfanns en ny typ av extrem ultraviolett laser, med pulser med pulslängd i storleksordningen av attosekunder. Dessa laserpulser kan användas som en mycket snabb kamerablixt, för att spela in en slow motion-film av hur elektronerna rör sig. Från denna slow motion-film är det möjligt att lära sig hur ljus interagerar med materia.

När en atom absorberar en foton med tillräckligt hög energi kan en elektron avlägsnas från atomen. Denna effekt kallas den fotoelektriska effekten. I detta examensarbete har jag använt en attosekundlaser för att mäta dynamiken av den fotoelektriska effekten för olika grundämnen.

Kvantmekanik är teorin som beskriver hur materia interagerar med ljus. Inom kvantmekaniken kan objekt ha märkliga egenskaper som är ointuitiva för makroskopiska varelser. Till exempel kan kvantobjekt vara på två ställen samtidigt, en egenskap som kallas superposition. Dessutom kan kvantobjekt vara sammanflätade, vad Einstein kallade, en spöklik växelverkan. Om två objekt, A och B, är sammanflätade, kommer en observation på A att ändra tillståndet för B omedelbart, även om de är åtskilda med ett stort avstånd. I denna avhandling presenteras en metod för att mäta kvanttillståndet hos en fotoelektron. Dessa mätningar gör det möjligt att karakterisera elektronens kvanttillstånd och kan skapa en förståelse för hur sammanflätningen beter sig mellan elektronen och atomen under dessa mycket korta tidsskalor.

Man kan hävda att arbetet med denna avhandling är av liten praktisk nytta. Grundforskning har dock upprepade gånger visat en förmåga att ge oväntade praktiska tillämpningar.

List of Publications

This thesis is based on the following publications, referred to by their Roman numerals:

- I Attosecond photoionization dynamics in the vicinity of the Cooper minima in argon**
C. Alexandridi, D. Platzter, L. Barreau, D. Busto, S. Zhong, M. Turconi, L. Neoricic, **H. Laurell**, C. L. Arnold, A. Borot, J.-F. Hergott, O. Tcherbakoff, M. Lejman, M. Gisselbrecht, E. Lindroth, A. L’Huillier, J. M. Dahlström, and P. Salières
Physical Review Research **3**, (2021)
- II Attosecond electron–spin dynamics in xe 4d photoionization**
S. Zhong, J. Vinbladh, D. Busto, R. J. Squibb, M. Isinger, L. Neoričić, **H. Laurell**, R. Weissenbilder, C. L. Arnold, R. Feifel, J. M. Dahlström, G. Wendin, M. Gisselbrecht, E. Lindroth, and A. L’Huillier
Nature Communications **11**, (2020)
- III Resonant two-photon ionization of helium atoms studied by attosecond interferometry**
L. Neoricic, D. Busto, **H. Laurell**, R. Weissenbilder, M. Ammitzböll, S. Luo, J. Peschel, H. Wikmark, J. Lahl, S. Maclot, R. J. Squibb, S. Zhong, P. Eng-Johnsson, C. L. Arnold, R. Feifel, M. Gisselbrecht, E. Lindroth and A. L’Huillier
Frontiers in Physics **05**, (2022)
- IV Breaking the time symmetry of Fano resonances in attosecond photoelectron interferometry**
S. Luo, R. Weissenbilder, **H. Laurell**, R. Y. Bello Romero, C. Marante, M. Ammitzböll, L. Neoričić, A. Ljungdahl, R. J. Squibb, R. Feifel, M. Gisselbrecht, C. L. Arnold, F. Martín, E. Lindroth, L. Argenti, D. Busto, A. L’Huillier
Manuscript in preparation

V Probing electronic decoherence with high-resolution attosecond photoelectron interferometry

D. Busto, **H. Laurell**, D. Finkelstein-Shapiro, C. Alexandridi, M. Isinger, S. Nandi, R. Squibb, M. Turconi, S. Zhong, C. Arnold, R. Feifel, M. Gisselbrecht, P. Salières, T. Pullerits, F. Martín, L. Argenti and A. L’Huillier

The European Physical Journal D **76**, (2022)

VI Continuous-variable quantum state tomography of photoelectrons

H. Laurell, D. Finkelstein-Shapiro, C. Dittel, C. Guo, R. Demjaha, M. Ammitzböll, R. Weissenbilder, L. Neoričić, S. Luo, M. Gisselbrecht, C. L. Arnold, A. Buchleitner, T. Pullerits, A. L’Huillier, and D. Busto

Physical Review Research **4**, (2022)

VII Ultra-stable and versatile high-energy resolution setup for attosecond photoelectron spectroscopy

S. Luo, R. Weissenbilder, **H. Laurell**, M. Ammitzböll, V. Poulain, D. Busto, L. Neoričić, C. Guo, S. Zhong, D. Kroon, R. J. Squibb, R. Feifel, M. Gisselbrecht, A. L’Huillier and Cord L. Arnold

Advances in Physics **X**, Submitted

VIII Measuring the quantum state of a photoelectron

H. Laurell, S. Luo, R. Weissenbilder, M. Ammitzböll, V. Poulain, C. Guo, S. Ahmed, A. F. Kockum, C. L. M. Petersson, E. Lindroth, C. Dittel, R. J. Squibb, R. Feifel, M. Gisselbrecht, C. L. Arnold, A. Buchleitner, A. L’Huillier, D. Busto

Manuscript in preparation

All papers are reproduced with permission of their respective publishers.

Abbreviations

APT	Attosecond Pulse Train
ATI	Above-Threshold Ionization
CPA	Chirped Pulse Amplification
DC	Direct Current
EWP	Electron Wave Packet
HHG	High-order Harmonic Generation
IR	Infrared
MCP	Micro Channel Plate
RABBIT	Reconstruction of Attosecond Beating by Interference of two-photon Transitions
SNR	Signal-to-Noise Ratio
Ti:Sapphire	Titanium:Sapphire
XUV	Extreme Ultraviolet
QST	Quantum State Tomography
MBES	Magnetic Bottle Electron Spectrometer
VMI	Velocity Map Imaging
RRPA	Relativistic Random Phase Approximation
RRPAE	Relativistic Random Phase Approximation with Exchange

Contents

Abstract	i
Popular Science Summary	iii
Populärvetenskaplig sammanfattning	v
List of Publications	vii
Abbreviations	ix
 Part I: Summary	 1
1 Introduction	1
1.1 Attosecond science	1
1.2 Quantum coherence in attosecond metrology	2
1.3 Outline	3
 2 Attosecond light pulses and High order harmonic generation	 5
2.1 Ultrashort light pulses	5
2.2 High order harmonic generation	10
2.3 Temporal structure of the emitted radiation	15
2.4 Light source of the attosecond laboratory	17
 3 Attosecond photoelectron interferometry	 19
3.1 Photoelectron interferometry	19
3.2 Reconstruction of attosecond beating by interference of two photon transitions (RABBIT)	24
3.3 Setup	28
3.4 Resolution	33
3.5 Results I: Time-delays	34
3.6 Results II: Resonances	38
 4 Quantum state tomography and decoherence in photoionization	 47
4.1 Introduction	47
4.2 KRAKEN	48
4.3 Electron purity and bipartite entanglement	50
4.4 Numerical simulations close to Fano resonances	53
4.5 Experimental setup	55

4.6	Experimental results	58
5	Summary and outlook	63
5.1	Summary	63
5.2	Outlook	65
	Author Contributions	67
	Acknowledgments	70
	References	73
Part II:	Publications	80
	Paper I: Attosecond photoionization dynamics in the vicinity of the Cooper minima in argon	81
	Paper II: Attosecond electron–spin dynamics in xe 4d photoionization	89
	Paper III: Resonant two-photon ionization of helium atoms studied by attosecond interferometry	97
	Paper IV: Breaking the time symmetry of Fano resonances in atto- second photoelectron interferometry	111
	Paper V: Probing electronic decoherence with high-resolution atto- second photoelectron interferometry	121
	Paper VI: Continuous-variable quantum state tomography of photo- electrons	133
	Paper VII: Ultra-stable and versatile high-energy resolution setup for attosecond photoelectron spectroscopy	149
	Paper VIII: Measuring the quantum state of a photoelectron	163

Chapter 1

Introduction

1.1 Attosecond science

To gain insight into a physical process it is necessary to measure its evolution. For example, the trajectory of a moving object can be recorded with a camera, from which the dynamics of the motion can be inferred. However for dynamics much faster than the duration of a flash of the camera it becomes impossible to understand the dynamics of the interaction. In the early 19th century stroboscopic photography were pioneered by Harold Edgerton [1] to study the dynamics of fast classical processes. In stroboscopic measurements a short light flash illuminates the object at a certain time of the evolution and the picture is recorded. This process is then repeated for different times enabling the reconstruction of the dynamics of the process. Stroboscopic measurements are ultimately limited to the pulse duration of the flash, so to study ever faster dynamics shorter light pulses are needed.

The intrinsic dynamics of chemistry occurs on extremely short timescales. The quantum beating period resulting from interference between two states separated in energy by ΔE is equal to, $\tau_{\text{beating}} = h/\Delta E$, where h is the Planck constant. This gives the time scale of the rotational motion of molecules to be on the order of picoseconds (10^{-12} s), vibrational molecular motion on the order of femtoseconds (10^{-15} s) and the electronic motion on the order of attoseconds (10^{-18} s).

With the advent of high harmonic generation [2, 3] and attosecond pulses [4, 5], attosecond light pulses could be used as flashes in measurements similar to stroboscopic measurements to measure how electron motion evolves on its

natural timescale. A common approach is to use an attosecond pulse to initiate the dynamics and then probe the dynamics with an infrared (IR) femtosecond pulse.

In this thesis an interferometric technique, Reconstruction of Attosecond Beating By Interference of Two photon transitions (RABBIT), has been used where an attosecond pulse train ionizes a sample and an IR femtosecond pulse probes the ionization dynamics. In RABBIT both the spectral amplitude and phase of the ionized photoelectron is measured, from which the dynamics of ionization can be retrieved.

Attosecond metrology has increased the knowledge of electron dynamics and using RABBIT photoionization dynamics has been measured in atoms [6–11], molecules [12–15] and solids [16, 17].

1.2 Quantum coherence in attosecond metrology

Recently, the fields of quantum information and attosecond physics have started to merge as questions regarding the coherence of electronic processes on the attosecond and femtosecond timescales have been posed. Coherence is the ability of quantum systems to maintain their quantum properties. As a quantum system interacts with its environment it is subject to decoherence and loses its quantum behaviour.

Entanglement and coherence have been studied in several recent works in attosecond science. In [18], the density matrix of an attosecond pulse train is measured from which the degree coherence of the pulse train is obtained. In [19], the degree of coherence of vibrational modes of H_2 is controlled and measured, effectively controlling the degree of entanglement between the ion and the photoelectron. Optical cat states have been generated using high order harmonic generation [20]. The density matrix of an electronic attosecond pulse train in the context of electron microscopy has been measured [21]. Additionally, entanglement between photoelectrons in non-sequential double ionization has been measured [22].

In this thesis we contribute to this development. We present a quantum state tomography protocol for photoelectrons (KRAKEN). Using KRAKEN it is possible to quantify the degree of coherence of a photoelectron, making it possible to address questions regarding the entanglement between the photoelectron and the ion. We present the first KRAKEN measurements in helium, neon and argon, where in the case of neon and argon we are able to quantify the degree of

entanglement between the ion and the photoelectron.

KRAKEN is a new measurement scheme that can address questions in photoionization dynamics, such as coherence and entanglement, that RABBIT could not. KRAKEN is therefore an useful new tool in attosecond scientists toolbox for studying attosecond dynamics in atoms, molecules, and solids.

1.3 Outline

In this thesis, photoionization dynamics is studied using the measurement techniques RABBIT and KRAKEN. The thesis summarizes the results of 8 papers.

In papers **I** and **II**, photoionization time-delays are measured using RABBIT. In particular, electron correlation is studied in argon and xenon. In argon, a broad spectral region covering the $3s$ and $3p$ Cooper minima, where the $3p$ amplitude is strongly reduced, is explored. In xenon, we study ionization in the $4d$ -shell covering part of the “giant dipole resonance” [23, 24].

In papers **III**, **IV** and **V** resonant photoionization dynamics is studied using RABBIT. In paper **III** the $1s3p$, $1s4p$ and $1s5p$ below threshold resonances in He are studied using angular resolved and angular integrated measurements. The angular resolved measurements show phase jumps in emission angle and kinetic energy that we then explain using perturbation theory. In paper **IV** the $3s^{-1}4p$ Fano resonance in argon is studied using angular integrated measurements. Due to the high spectral resolution of the electron spectrometer and the narrow IR probe spectra we are able to resolve a larger than π phase variation. The large phase variation is attributed to the complexification of the Fano parameter, q . In paper **V** angularly integrated RABBIT measurements are used to study the $2s2p$ Fano resonance in helium. The amplitude and phase are measured across the resonance from which the density matrix and Wigner function of the photoelectron is reconstructed.

In paper **VI** the KRAKEN protocol is presented. In KRAKEN a narrowband bichromatic probe field is used to retrieve subdiagonals of the photoelectron density matrix, and subsequently by scanning on of the wavelengths of the probe the full density matrix can be reconstructed. We validate the KRAKEN protocol using numerical simulations and reconstruct the density matrices of photoelectrons emitted in the vicinity of the $2s2p$ and $3s^{-1}4p$ Fano resonances in helium and argon, showing excellent agreement with theoretical calculations. In paper **VII** we present a new photoelectron interferometer for RABBIT and KRAKEN measurements. The interferometer is versatile, has high spectral res-

olution and excellent temporal stability. Finally, in paper **VIII** we experimentally demonstrate the KRAKEN protocol in helium, neon and argon showing excellent agreement with theoretical calculations. We measure a purity less than one in the case of neon and argon which implies that the ion and the photoelectron are entangled.

The introduction to the articles is structured as follows: in chapter **2**, the concepts of high-order harmonic generation and attosecond pulses are introduced. Furthermore, the laser system used for the measurements in this thesis is presented. In chapter **3** attosecond time-delays and photoelectron interferometry is introduced. More specifically, the RABBIT protocol is derived using a density matrix formalism. In chapter **4** the quantum state tomography protocol, KRAKEN, is presented. Additionally, how to characterize ion-photoelectron entanglement using KRAKEN is explained. We present a summary and outlook in chapter **5**.

Chapter 2

Attosecond light pulses and High order harmonic generation

2.1 Ultrashort light pulses

This chapter introduces the mathematical description of optical pulses. A brief summary on ultrafast laser development is made and the concept of high order harmonic generation is introduced.

2.1.1 Waveforms and optical pulses

An optical pulse can be represented by its complex amplitude,

$$E(t) = A(t)e^{i\phi(t)}. \quad (2.1)$$

Where $A(t)$ is the temporal envelope of the pulse and $\phi(t)$ the phase. $A(t)$ and $\phi(t)$ are real scalar functions. Optical pulses are square-integrable, i.e. they have finite energy. It is therefore well defined to take the Fourier transform of a pulse $E(t)$, and get the spectral amplitude of the pulse as,

$$E(\omega) = \frac{1}{2\pi} \int_{-\infty}^{\infty} dt A(t)e^{i\phi(t)+i\omega t}. \quad (2.2)$$

Since optical pulses have a well defined Fourier transform the temporal and spectral variance obey the Fourier uncertainty relation, also denoted the time-bandwidth product,

$$\Delta\omega\Delta t \geq \frac{1}{4\pi}. \quad (2.3)$$

This relation can be shown by using the definition of the variances $\Delta\omega$ and Δt . For Gaussian pulses, the Fourier uncertainty is minimal. Expressed in full width at half maximum (FWHM) and frequency (ν), using that $\nu = \omega/2\pi$, the uncertainty becomes,

$$\Delta t_{FWHM}\Delta\nu_{FWHM} \geq 0.44. \quad (2.4)$$

A consequence of the Fourier uncertainty principle is the Heisenberg uncertainty principle of quantum mechanics. Due to the wave-particle duality, first introduced by de Broglie, and the Fourier transform relationship between the canonical conjugates, such as the position and momentum observables (\hat{x}, \hat{p}) the Heisenberg uncertainty principle is enforced,

$$\Delta x\Delta p \geq \frac{h}{4\pi}. \quad (2.5)$$

A difference between the Fourier uncertainty and the Heisenberg uncertainty is the introduction of the Planck constant. The Planck constant originates from the canonical quantization procedure and the commutator between the canonical conjugates. The meaning of the Heisenberg uncertainty is as follows. An observation of a canonical quantity restricts the variance of the canonical conjugate. If the position representation of a quantum state is confined, then the momentum representation is uncertain and vice versa. This uncertainty holds for all observables with canonical conjugates. It was shown by Pauli, that there is no observable for time. However, it is still possible to reformulate the Heisenberg uncertainty principle in energy and time,

$$\Delta E\Delta t \geq \frac{h}{4\pi}. \quad (2.6)$$

For short temporal intervals, the energy of a quantum state is uncertain. Imagine that you are customer at a quantum mechanical bank. Contrary to what is possible at a classical bank, you can at the quantum bank withdraw more than is in your account given that you deposit it again quickly enough. This strange structure of reality enables physical phenomena such as virtual particles and vacuum fluctuations. Returning to optical pulses, the most common optical

waveform is probably the Gaussian pulse. It is defined as,

$$E(t) = A_0 \exp \left(-\frac{t^2}{2\sigma_t^2} + i\omega_c t + i\phi(t) \right), \quad (2.7)$$

where σ_t characterizes the temporal width of the pulse, ω_c the carrier frequency and $\phi(t)$ the temporal phase. If the temporal phase $\phi(t)$ is constant or linear, the Fourier uncertainty is exact and the pulse is what is called Fourier limited. If not, the pulse is chirped. A chirp implies that the instantaneous frequency varies as function of time as

$$\omega_i(t) \equiv \frac{\partial \text{Arg}(E(t))}{\partial t} = \omega_c + \frac{\partial \phi(t)}{\partial t}. \quad (2.8)$$

If the temporal phase is constant, it contributes to the pulse as a global phase shift and the instantaneous frequency is invariant. A linear temporal phase results in a constant shift of the instantaneous frequency. Since the instantaneous frequency is dependent on the derivative of the temporal phase, a linear spectral chirp has a quadratic temporal phase. Chirped pulses are not Fourier limited. A visualization of the concept of spectral chirp is given in Fig. 2.1. It is possible to

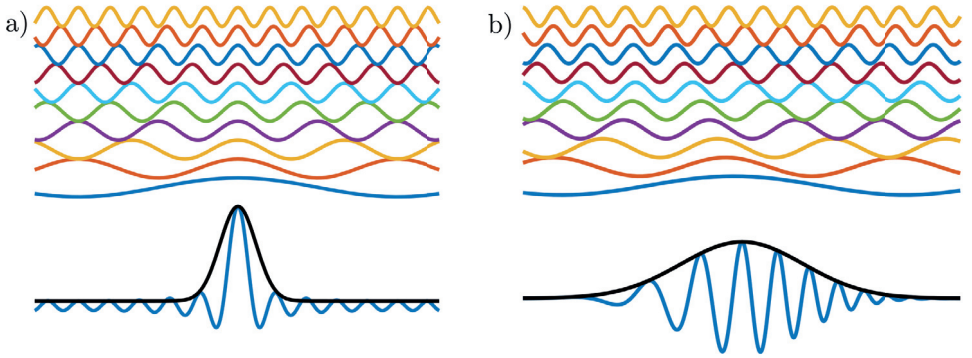


Figure 2.1: a) Fourier limited pulse, the spectral components are phase locked and arriving at the same time. b) Pulse with a linear spectral chirp, the spectral components arrive with a quadratic lag proportional to their frequency.

represent a waveform in the spectral and temporal domain simultaneously using time-frequency analysis. In linear time-frequency analysis instead of taking the Fourier integral over all times, a window function is applied that localizes the observation to a temporal interval. A common linear time-frequency represent-

ation is the short-time Fourier transform (STFT),

$$S(\omega, \tau, \sigma) = \frac{1}{2\pi} \int_{-\infty}^{\infty} dt E(t) h(t - \tau, \sigma) e^{i\omega t}. \quad (2.9)$$

For the short-time Fourier transform, $h(t - \tau, \sigma)$ is a rectangular window function. Different choices of window function will give different time-frequency representations of the waveform. For example, using the Gaussian function as window function defines the Gabor transform. Linear time-frequency representations are the most common approach for analyzing signals in the time-frequency domain. However, in some situations higher-order time-frequency representation can be advantageous. Perhaps the most famous second-order time-frequency representation is the Wigner-Ville representation [25–27],

$$W_f(\omega, t) = \int_{-\infty}^{\infty} d\tau E^* \left(t - \frac{\tau}{2} \right) E \left(t + \frac{\tau}{2} \right) e^{i\omega t}. \quad (2.10)$$

The Wigner function is a quadratic time-frequency representation and has higher temporal-spectral resolution than a linear time-frequency representation, such as the STFT [27]. However the Wigner function intrinsically is subject to self-interference which can be problematic for some applications. The Wigner function [25] is also a central object in the phase-space formulation of quantum mechanics where it is the phase space representation of the density matrix and is defined as,

$$W_f(x, p) = \int_{-\infty}^{\infty} d\xi \left\langle x - \frac{\xi}{2} \right| \hat{\rho} \left| x + \frac{\xi}{2} \right\rangle e^{i\xi p}. \quad (2.11)$$

A general density matrix $\hat{\rho}$ can be written as $\sum_k p_k |k\rangle \langle k|$ and p_k are the probabilities of the projectors, $|k\rangle \langle k|$. Inserting two completeness relations and thus representing the Wigner function in the position representation gives,

$$W_f(x, p) = \sum_k p_k \int_{-\infty}^{\infty} d\xi \psi_k^\dagger \left(x - \frac{\xi}{2} \right) \psi_k \left(x + \frac{\xi}{2} \right) e^{i\xi p}, \quad (2.12)$$

which for a pure state reduces to,

$$W_f(x, p) = \int_{-\infty}^{\infty} d\xi \psi^\dagger \left(x - \frac{\xi}{2} \right) \psi \left(x + \frac{\xi}{2} \right) e^{i\xi p}, \quad (2.13)$$

showing that the Wigner function of a pure state has the same form as the Wigner-Ville time-frequency representation.

2.1.2 Chirped pulse amplification

Since the invention of the first laser by Theodore Maiman in 1960 [28], the use and applications of laser technology has been extensive. It has since its inception been an essential technology in industrial manufacturing and research.

In Fig 2.2 the development of focused laser intensity over time is shown. Between 1960 and 1970, Q-switching and mode-locking [29, 30] were invented. Q-switching and mode-locking enabled the laser to be pulsed, confining the pulse energy in a short temporal window. This increased the focused intensity several orders of magnitude. Between 1970 and 1985, the focused intensity stagnated due to damage of the amplification medium at high pulse intensity. The optical break-

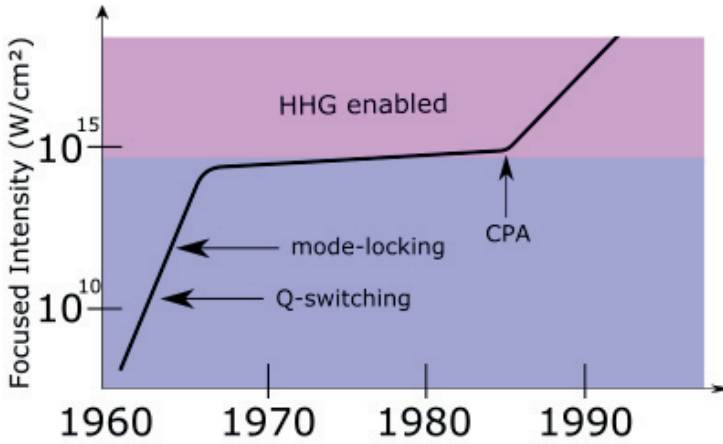


Figure 2.2: Development of focused intensity over time. Figure adapted from [31].

down of the gain medium was a problem that Donna Strickland and Gerard Mourou faced, and subsequently solved in 1985 by inventing the chirped pulse amplification (CPA) scheme [32]. For this invention they were awarded the 2018 Nobel prize in physics. In CPA, a clever trick is used to circumvent the high intensities in the gain medium, that ultimately leads to optical breakdown. An overview of CPA in the time-domain is shown in Fig. 2.3. The main idea is to start with low intensity ultra-short pulses generated in an oscillator. In the following description of CPA the pulse duration and pulse energies are the ones that were used in this work. The short pulses are generated by mode-locking.

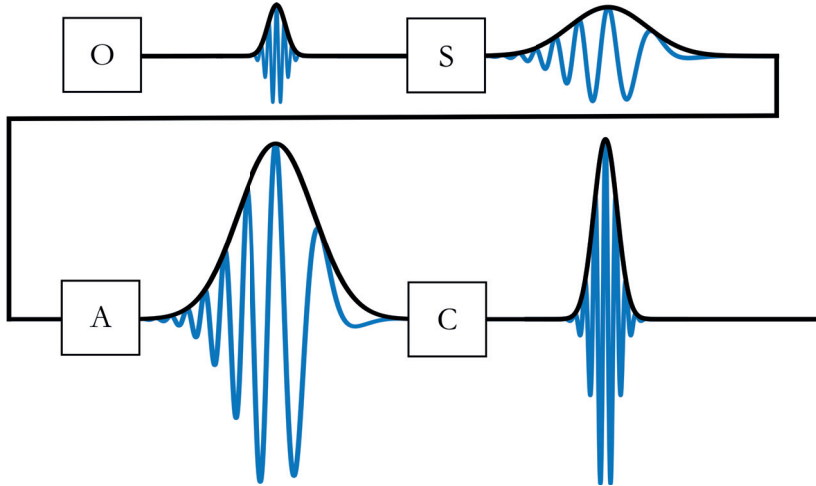


Figure 2.3: Schematic over a chirped pulse amplifier in the temporal domain. An oscillator (O) delivers a short and weak pulse that is temporally stretched in a stretcher (S) after which it is amplified (A) and finally compressed (C).

The pulses are then sent through a stretcher. This is an optical configuration, commonly using dispersive elements, such as prisms or gratings, that increase the pulse duration by applying a spectral chirp. This dispersion ideally preserves the pulse energy but stretches the pulse in time, according to the Fourier uncertainty principle, from 20 fs to often hundreds of picoseconds. This dramatically decreases the intensity of the pulse. After the stretcher, the pulse is amplified, often through a sequence of optical amplifiers. Due to the long temporal trace of the pulse, the pulse energy can be increased by many orders of magnitude without optical breakdown of the medium. Finally, the pulses are compressed in a compressor which is the optical inverse operation of the stretcher. The compressor output is a laser pulse with a similar pulse duration as the original pulse of 20 fs, but with an energy on the order of mJ.

The incredible breakthrough by Strickland and Mourou started a new era of laser development and new light sources based on non-linear optics took advantage of the dramatic increase in pulse energy.

2.2 High order harmonic generation

High order harmonic generation is a highly nonlinear optical process that can occur when a high intensity laser pulse, often generated through CPA, is focused

down in a medium, most commonly an atomic gas. In the focus of the laser beam the peak intensity can reach intensities on the order of PW/cm^2 giving an electric field strength of the light on the order of GV/cm , comparable to the electric field of the atomic potential. The strong optical field greatly distorts the Coulomb potential and enables highly non-linear processes. Subsequently, optical overtones of the fundamental laser field are emitted from the medium forming a harmonic spectrum where the harmonics, of odd order, are separated from each other by twice the frequency of the driving field.

Similarly to when a pianist strikes a note, overtones are generated and the intensity of the overtones decreases rapidly with increasing harmonic order. However, for the optical high order harmonic generation process this describes only the perturbative regime. For optical high order harmonics something very strange happens. At high harmonic orders, the intensity of the harmonics stops decreasing and can remain almost constant for many harmonic order. This region is called the plateau and can only be described non-perturbatively. At a high harmonic order the harmonic intensity sharply drops defining what is denoted the harmonic cutoff. Figure 2.4 shows a schematic of a harmonic spectrum with the perturbative, non-perturbative and cutoff regions indicated. High order har-

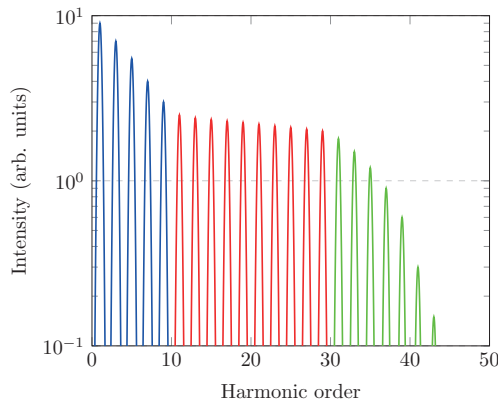


Figure 2.4: Schematic of a harmonic spectrum showing three regions. (Blue peaks) The perturbative region, here the intensity of the harmonics decreases rapidly as function of harmonic order. (Red peaks) The plateau/non perturbative region, the intensity of the harmonics is constant as function of harmonic order. (Green peaks) The cutoff, for energies greater than $3.17U_p$ the harmonic intensity decrease with increasing harmonic order.

monic generation was first demonstrated by [2, 3] and has then since sparked much research activity due to the possibility to generate table top coherent sources of pulses with attosecond duration and spectrum in the XUV and soft x-ray spectral range, which are of interest in spectroscopy and XUV metrology

[5].

2.2.1 The three step model

Due to the non-perturbative nature of the plateau harmonics, perturbation theory cannot be used to explain them. A full quantum model of HHG based on solving the time-dependent Schrödinger equation was developed in [33]. Additionally, a semi-classical model called the three step model was developed in [34, 35]. The three step model treats the tunneling through the atomic potential quantum mechanically and the propagation of the tunnel-ionized electron classically. It describes well the physics of high order harmonic generation. More advanced theoretical descriptions exist, such as the strong field approximation (SFA) [36]. However, in this thesis emphasis will be put on the three step model.

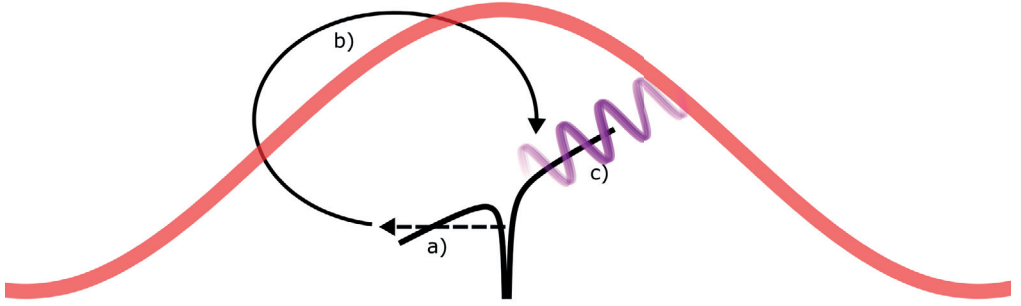


Figure 2.5: Illustration of the three step model. a) Tunneling ionization of a dressed atom. b) Propagation of the electron in the continuum. c) Recombination and emission of a high energy photon.

A schematic of the three step model is shown in Fig. 2.5. In the three step model the atomic potential is perturbed by a driving optical field. If the electric field strength of the optical field is of the same order of magnitude as the atomic potential, it perturbs the potential to such an extent that tunneling ionization is allowed. Since there exists a probability for the valence electron to tunnel through the atomic potential, a process called tunneling ionization, the electron will tunnel-ionize. It is assumed to have zero velocity in the continuum after tunneling. Thereafter the driving field accelerates the ionized electron classically. After a half-cycle, the optical driving field switches sign and the electron is decelerated and subsequently accelerated back to the ion. When the electron is back in close proximity of the ion there is a small but finite probability of recombination. If the electron recombines, through the conservation of energy

a high energetic photon will be emitted with energy,

$$E_{\text{photon}} = I_p + T_{\text{electron}}, \quad (2.14)$$

where I_p is the ionization potential of the target atom, and T_{electron} the kinetic energy of the electron at recombination. The ionization potential is dependent on the target atom and is generally of the order of tens of eV. For xenon the ionization potential is 12.1 eV and for helium 24.6 eV. Treating the driving field classically, $E = E_0 \sin \omega t$, and solving the equations of motion, the radial position of the electron for times $t \geq t_i$, where t_i is the time that the electron tunnels, can be found as,

$$x(t) = \frac{qE_0}{m_e\omega^2} \left(\sin(\omega t) - \sin(\omega t_i) - \omega(t - t_i) \cos(\omega t_i) \right), \quad (2.15)$$

where q is the electron charge, E_0 the electric field amplitude, m_e the mass of the electron, and ω the angular frequency of the driving field. In Fig. 2.6, the

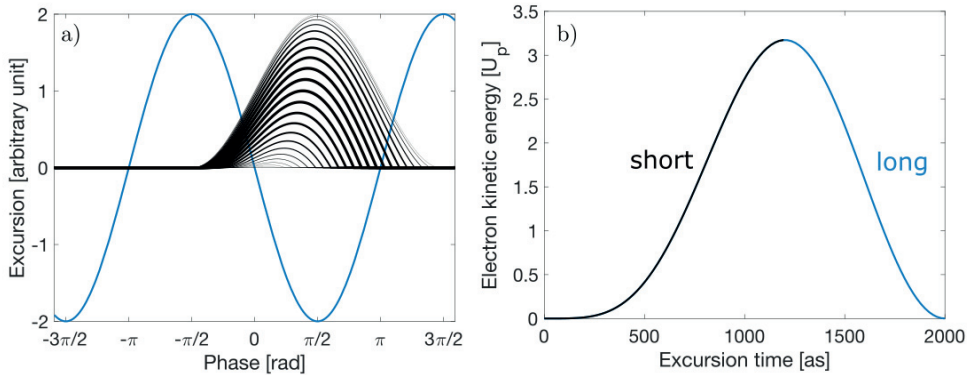


Figure 2.6: a) Classical electron trajectories in black. The return energy is encoded in the linewidth of the curves. In blue the driving optical field. b) Electron kinetic energy vs. excursion time. Two trajectories end up with the same final kinetic energy.

electron trajectories are shown and the electron kinetic energy at recombination is shown vs. excursion time. The maximal kinetic energy that the electron can acquire is $3.17U_p$, where U_p is the ponderomotive energy given by,

$$U_p = \frac{E_0^2 q^2}{4m_e\omega^2} \propto \lambda^2 I_0, \quad (2.16)$$

where I_0 is the peak intensity and λ the laser wavelength. This defines the cutoff

of the high harmonic spectra as,

$$E_{\text{photon}}^{\text{cutoff}} = I_p + 3.17U_p. \quad (2.17)$$

Since U_p is proportional to the square of the wavelength and the intensity of the driving field, the cutoff of the harmonic spectra can be extended to higher energies either by using laser sources with longer wavelengths (or increasing the intensity of the driving field, however this approach is ultimately limited by the ionization of the medium). This has sparked the recent wave of table-top soft x-ray sources [37] using HHG generated from mid-IR lasers with longer fundamental wavelength than the traditional Ti:Sapphire with a wavelength of 800 nm. The HHG conversion efficiency scales approximately in the range $(\lambda^{-5} - \lambda^{-9})$ [38, 39] making it challenging to build such sources.

For a given kinetic energy the recombination time is not unique, corresponding to different times in the continuum. Two trajectories for the electron are possible. These trajectories are denoted as long and short and were first experimentally verified in [40]. The emitted XUV pulse will after recombination inherit the properties of the electron wavepacket including its chirp.

2.2.2 Phase matching

So far in the description of HHG we have considered the single atom response. In reality the gas medium is not localized to a single point in space and the intense laser pulse does not interact with a single atom but an ensemble of atoms at random positions in space [41]. If the phase relation from all these point sources is random the emitted radiation will average out to zero, dramatically decreasing the conversion efficiency of the generation process. To mitigate this, a phase relationship must be enforced between the point sources. This enforcement is called phase matching and for HHG is described by equation [42],

$$\Delta\bar{k}(q) = q\bar{k} - \bar{k}_q = 0, \quad (2.18)$$

where \bar{k} is the wave vector of the IR field and \bar{k}_q is the wave vector of the XUV field with frequency $q\omega$. Phase matching is fulfilled when the wave vector mismatch, $\Delta\bar{k} = 0$. $\Delta\bar{k}$ can be decomposed into,

$$\Delta\bar{k} = \Delta\bar{k}_{\text{dipole}} + \Delta\bar{k}_{\text{free electrons}} + \Delta\bar{k}_{\text{neutral atoms}} + \Delta\bar{k}_{\text{Gouy}}. \quad (2.19)$$

The dipole phase $\Delta\bar{k}_{\text{dipole}}$ describes the phase acquired by the electron while propagating in the continuum before recombination. The terms $\Delta\bar{k}_{\text{free electrons}}$

and $\Delta\bar{k}_{\text{neutral atoms}}$ describe the contributions to the refractive index of the medium due to ionized electrons, a negative contribution, and neutral atoms a positive contribution. The last term, $\Delta\bar{k}_{\text{Gouy}}$, describes the Gouy phase variation across a focus of an optical beam.

2.3 Temporal structure of the emitted radiation

After the demonstration of high order harmonic generation, the temporal structure of the generated light has been investigated. Given the large spectral bandwidth of tens to hundreds of eV, through the Fourier uncertainty, if the harmonics are phase locked it is possible to have pulses with pulse duration on the order of attoseconds [43, 44], yielding the shortest coherent pulses ever generated. Considering a spectral bandwidth of 100 eV, the Fourier limit becomes,

$$\Delta t \geq \frac{0.44}{\Delta\nu} = \frac{0.44h}{100 \text{ eV}} = 18.2 \text{ as.} \quad (2.20)$$

The lower bound of the pulse duration hold strictly for Fourier limited pulses, i.e. unchirped pulses.

To determine the pulse duration of the attosecond pulse a cross correlation technique called Reconstruction of Attosecond Beating By Two Photon Transitions (RABBIT), further discussed in chapter 3, was used. Through RABBIT measurements [4], it was found that the temporal structure of the pulses is an attosecond pulse train. Given a harmonic spectra of odd order harmonics, and representing the harmonics as a coherent sum of Dirac delta functions,

$$E(\Omega) = \sum_{n=0}^N A_n \delta(\Omega - \omega(2n+1)) \exp(i\phi_n). \quad (2.21)$$

After Fourier transformation of the spectra the temporal waveform becomes,

$$E(t) = \sum_{n=0}^N A_n \exp(i\omega(2n+1)t + i\phi_n). \quad (2.22)$$

Using RABBIT measurements, the phase difference of consecutive harmonics was measured [4], and shown to be approximately linear as function of XUV frequency,

$$\Delta\phi_{2n} = \phi_{2n+1} - \phi_{2n-1} \propto (2n+1). \quad (2.23)$$

This implies that the spectral phase is proportional to the square of the harmonic order,

$$\phi_{2n+1} \propto (2n+1)^2, \quad (2.24)$$

showing that the attosecond pulse train is not Fourier limited. However since both the spectral amplitude, A_n , and the phase, ϕ_n , can be measured it is possible to take the inverse Fourier transform and obtain the temporal structure as an attosecond pulse train, where the individual attosecond pulses are approximately 100 as long. If there is no phase relation between consecutive ϕ_n , the coherent sum of $E(t)$ becomes an incoherent sum and the temporal width an individual pulse in the pulse train is on the order of fs.

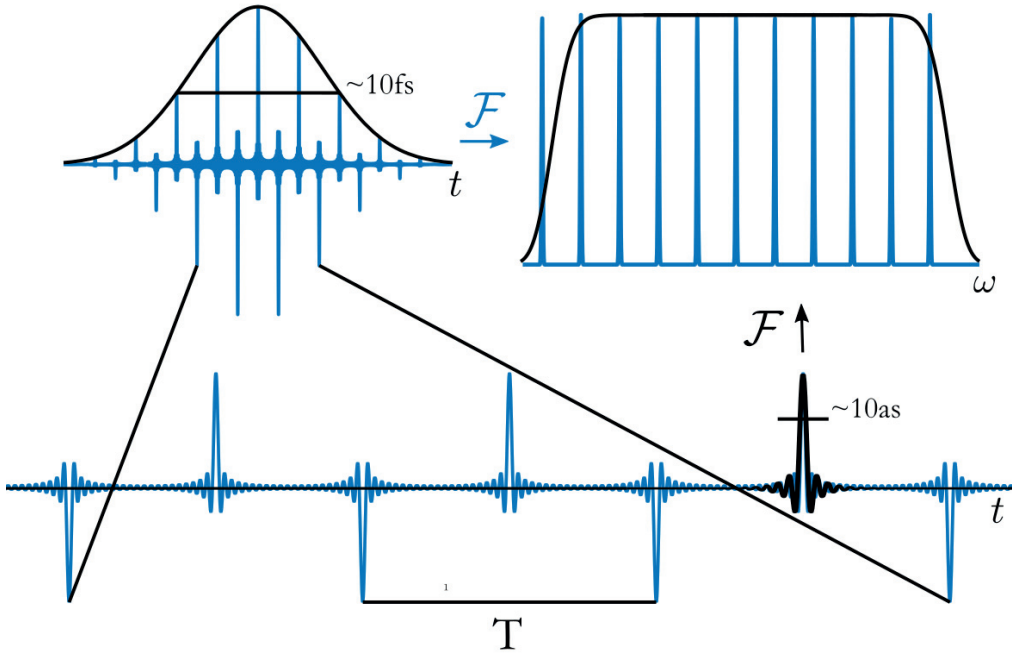


Figure 2.7: Temporal structure of the attosecond pulse train. Fourier transformation of the attosecond pulsetrain gives a spectrum with harmonics separated by 2ω . Fourier transformation of a single attosecond pulse gives a continuous spectra with the same spectral width as the pulse train.

In Fig. 2.7 a schematic representation of the temporal structure of the high order harmonics is shown. To summarize, in the time domain, the attosecond pulse train is a consequence of phase-locked harmonics. In the spectral domain

the harmonic spectra with spacing of 2ω , is a consequence of the temporal interference of attosecond pulses emitted every half-cycle of the driving field. If a single attosecond pulse is gated in the temporal domain this corresponds in the spectral domain to a continuous spectrum.

The discovery of high harmonic generation and attosecond pulses has enabled probing dynamics of electronic motion on the attosecond time scale, its natural time-scale. Opening the field of attosecond physics.

2.4 Light source of the attosecond laboratory

In this thesis attosecond pulse trains were generated using HHG driven by femto-second IR pulses. The laser used is a Ti:Sapphire CPA system with a central wavelength of 800 nm. A schematic of the laser system is shown in Fig. 2.8. The laser system has five main components, the oscillator, stretcher, regenerative amplifier, cryogenic amplifier and the compressor. The oscillator emits pulses with a power of 240 mW at 80 MHz repetition rate giving a pulse energy of 3 nJ. The oscillator spectrum spans from 650 to 950 nm. The spectrum is cut at the first mirror to span roughly from 700 to 900 nm, where 90 mW of average power are sent into the stretcher. After the stretcher the pulses are sent through an programmable acousto-optic modulator (DAZZLER) that can control the spectral amplitude and phase of the pulses. After the DAZZLER the pulses are sent through a 4-pass booster amplifier, and then through a Pockels cell that picks pulses with a repetition rate of 1 kHz and transmits them into the regenerative amplifier. In the regenerative amplifier the pulses are amplified in 14 round trips giving a final pulse energy of 0.4 mJ after which the pulse is coupled out with a secondary Pockels cell. The pulse is then sent into a three-pass amplifier which increases the pulse energy to 4 mJ and subsequently sent into the three-pass cryogenically cooled amplifier. The final amplification stage increases the pulse energy to 7-10 mJ. All amplifiers are pumped with the second harmonic of Neodymium-doped yttrium lithium fluoride pump lasers (Nd:YLF) with a central wavelength of 527 nm. After the cryo amplifier the pulses are compressed in a compressor back to close to the Fourier limit with an efficiency of 65% giving a final pulse energy of 4.5-6.5 mJ and a pulse duration of 22 fs. These laser pulses were used to generate, through HHG, the attosecond pulse train in paper **I**, **II**, **V** and in the angle-resolved measurements in paper **III**.

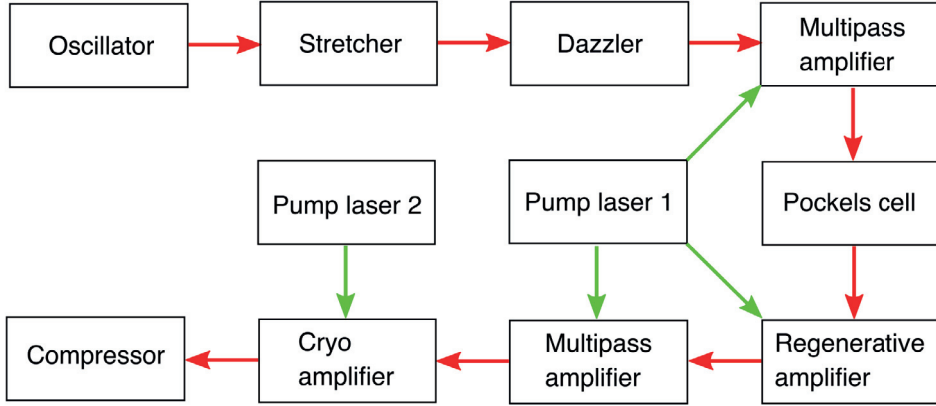


Figure 2.8: Schematic of the laser system in the attosecond laboratory. The laser system is a Ti:Sapphire CPA system.

The laser system was upgraded during my PhD, increasing the repetition rate and enabling to lock the carrier envelope phase (CEP) offset. New pump lasers enabled to increase the repetition rate of the laser system to 3 kHz while maintaining the pulse energy of 5 mJ and pulse duration of 22 fs. The upgraded laser system was used in the measurements for paper **IV**, **VIII** and in the angle integrated measurements in **III**.

Chapter 3

Attosecond photoelectron interferometry

In this chapter, we present the main part of the experimental results of this thesis (papers **I**, **II**, **III**, **IV**, **V**). The aim of the measurements is first introduced and more specifically the RABBIT technique is explained and derived using a density matrix approach. A new attosecond photoelectron interferometer is presented and finally attosecond photoelectron interferometry measurement results are presented.

3.1 Photoelectron interferometry

3.1.1 Atomic photoionization dynamics

Photoionization is the physical phenomena where an electron subject to electromagnetic radiation is removed from an atom and emitted into the continuum. For this to occur the photon energy must be greater than the ionization potential, $\hbar\omega > I_p$, or the intensity high enough to allow multi-photon processes such as multi-photon ionization (MPI) [45]. When the electron is bound to the atomic potential, the energy states that the electron can occupy are quantized. However after the ionization moment, leaving the atomic potential behind, the electron is described quantum mechanically with scattering states $|\epsilon_\alpha\rangle$, where ϵ represents the kinetic energy of the electron and α is a set of good quantum numbers. Asymptotically, these scattering states can be approximated by plane waves. An electron wavepacket is no longer well defined in energy but given as

a distribution. It is therefore represented as a superposition of scattering waves,

$$|\psi\rangle = \sum_{\alpha} \int d\epsilon \, c_{\alpha}(\epsilon) |\epsilon_{\alpha}\rangle \quad (3.1)$$

For a long time, only the amplitude of ionization was measurable using photoelectron spectroscopy. However with the advent of photoelectron interferometry, it became possible to measure both the spectral amplitude and relative phase of the electron wave packet after photoionization. Subsequently, by taking the Fourier transform of the measured electron spectral amplitude and phase it is possible to retrieve the corresponding temporal amplitude and phase of the photoelectron, enabling the study of photoionization dynamics in the time domain.

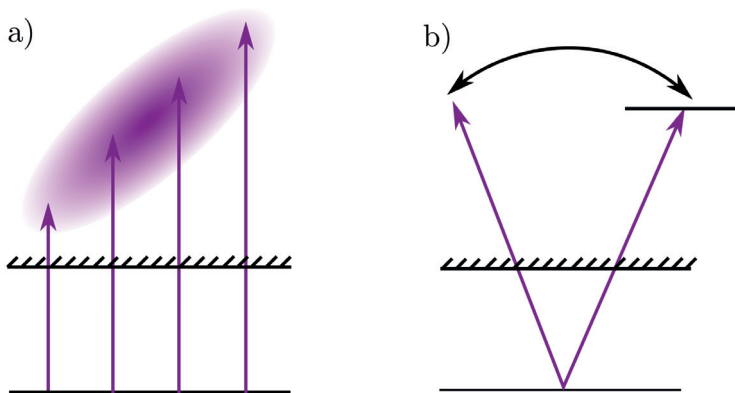


Figure 3.1: Broadband a) and narrowband b) EWP excited by HHG. The broadband EWP is localized in space and evolves on the as timescale, while the narrowband EWP evolves on the fs timescale.

The wavepacket can either be excited by a broadband XUV field consisting of many harmonics (Fig. 3.1 a)) or a single harmonic (Fig. 3.1 b)). The broadband EWP is initially localized in space and evolves on the attosecond (10^{-18} s) timescale while the narrowband EWP evolves on the (10^{-15} s) femtosecond timescale. The broadband EWP is used to measure ionization time-delays in paper **I**, **II** while the narrowband EWP is used to measure the amplitude and phase across atomic resonances in paper **III**, **IV**, **V**.

The Hilbert space of the scattering state is continuous, since the kinetic energy of the photoelectron can take on any positive value, and thereby of infinite

dimension. When the electron wave-packet leaves the potential of the parent ion it is subject to dispersion due to variation of the atomic potential as function of radial distance to the core. This concept was developed by Eisenbud, Wigner and Smith [46] and is commonly denoted the Wigner time-delay, τ_s . Wigner interpreted the spectral phase variation of the photoelectron as a time-delay encoding the photoionization dynamics. In a general scattering process the delay obtained by a wavepacket is given by,

$$\tau_s = 2\hbar \frac{\partial \phi}{\partial E}. \quad (3.2)$$

Fig. 3.2 shows a general scattering process. The wavepacket that scatters on the potential arrives on the other side before the wavepacket that does not.

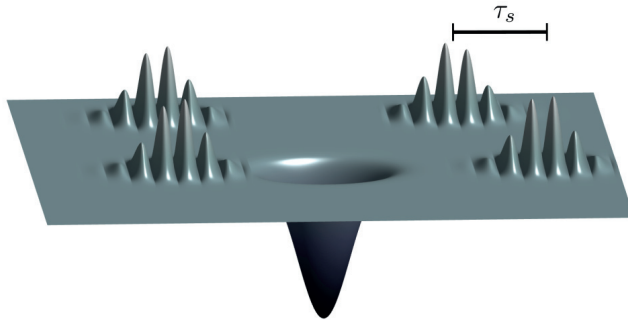


Figure 3.2: Scattering time delay induced wavepacket travelling through potential. The wavepacket travelling through the potential arrives faster at the other side than the wavepacket that does not.

In a Coulombic potential, the asymptotic limit of the radial continuum wavefunction of a scattering state with angular momentum L has the form [47],

$$\lim_{r \rightarrow \infty} R_{k,L}(r) = \sqrt{\frac{2}{\pi k r^2}} \sin \left(k r + \frac{Z \ln(2kr)}{k} + \eta_L(k) - \frac{\pi L}{2} \right), \quad (3.3)$$

where k is the wavevector, related to the kinetic energy as, $E = \hbar^2 k^2 / 2m$, r the radial distance to the core and Z is the nuclear charge. $\eta_L(k)$ is the

scattering phase and L the angular momentum. The scattering phase can be further decomposed in two contributions $\eta_L(k) = \sigma_L(k) + \delta_L(k)$, where $\sigma_L(k)$ is the Coulomb phase shift and $\delta_L(k)$ a phase shift introduced to compensate for the quantum defect. In photoionization, the derivative of $\eta_L(k)$ with respect to kinetic energy gives the scattering time-delay as half of the delay previously introduced,

$$\tau^{\text{EWP}} = \hbar \frac{\partial \eta_L(k)}{\partial E}. \quad (3.4)$$

The half comes from the fact that photoionization is a half scattering process with just an outgoing wave. The Wigner time-delay can be interpreted as the group delay of the electron wavepacket due to the effect of the short range potential. An interesting consequence of that the scattering states Hilbert space is bound from below is that it is not possible to define a conjugate operator for time, leaving time a parameter in quantum mechanics. This argument was first put forward by Pauli and is denoted the Pauli objection [48]. Therefore the Wigner delay should not be viewed as a temporal observable but as the derivative of the spectral phase or the group delay of the EWP. In general, the measurement of the spectral phase of photoelectrons over a large energy range (Fig. 3.1 a)) allows the study of photoionization dynamics through the measurement of the Wigner time-delay.

3.1.2 Fano resonances

The amplitude and phase of an electron wavepacket can have a large variation, if the ionization occurs through an atomic resonance, such as a Fano resonance. Fano resonance is a quantum interference phenomena between direct photoionization and ionization via a bound state, which autoionizes. Its theoretical description was given by Fano in 1961 [49]. Attosecond interferometry techniques have allowed the measurement of the amplitude and phase variation of the ionizing electron wavepacket (EWP) across the $3s^{-1}4p$ resonance in argon [8, 50, 51] and the doubly excited states ($2s2p$, $2s3p$) in helium [10, 52] and the $2s^{-1}np$ resonances in neon [53]. In particular, the build-up in time and frequency of the electron wave packet, around the $2s2p$ resonance has been characterized [10, 52]. The ultrafast dynamics the $2s2p$ Fano resonance has also been investigated using attosecond transient absorption [54]. Additionally using the same technique, Ott and coworkers have shown that it is possible to control the Fano lineshape with an intense IR pulse [55] and to observe the correlated two-electron dynamics in real time [56].

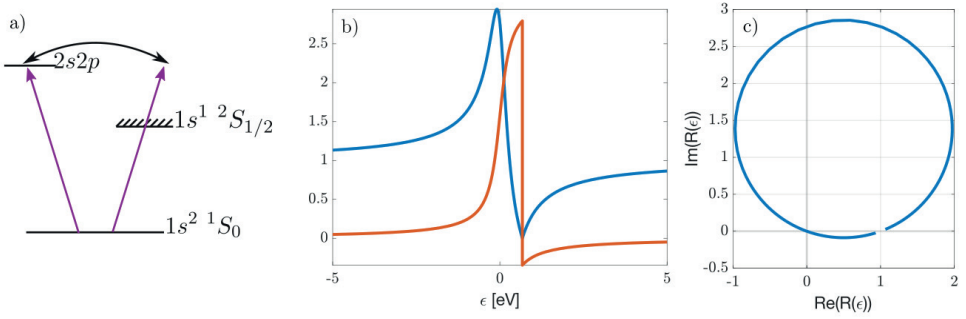


Figure 3.3: a) Energy diagram for the $2s2p$ Fano resonance in helium. b) Amplitude (blue curve) and phase (red curve) of the Fano resonance factor $R(\epsilon)$. c) Complex trajectory of the resonance factor. At the resonance energy the complex trajectory travels through the origin of the complex plane. Giving rise to the discontinuous π phase jump in $\text{Arg}(R(\epsilon))$.

Fig. 3.3 shows the energy diagram of the $2s2p$ Fano resonance in helium. Following absorption by an XUV photon, an electron can be excited from the ground state to the doubly excited state. Due to configuration interaction the electron after some time autoionizes to the continuum. Alternatively the electron can be directly ionized to the continuum following absorption of an XUV photon. Since there are two pathways that reach the same final state in energy, there will be quantum interference leading to the famous asymmetric Fano lineshape. Following the formalism of [57], the one photon interaction prepares the atom in the eigenstate,

$$|\psi_E\rangle = a_\phi |\phi\rangle + \int d\epsilon b(\epsilon) |\epsilon\rangle, \quad (3.5)$$

where the first term describes the bound state and the second term represents the continuum. The transition amplitude to the resonant continuum can then be calculated as,

$$\langle\psi_E|\hat{z}|g\rangle = \langle E|\hat{z}|g\rangle \frac{\epsilon + q}{\epsilon + i}, \quad (3.6)$$

where \hat{z} is the dipole operator and q is a real parameter that characterizes the resonance. It is given as the ratio between the transition matrix elements of the autoionizing and the direct channels,

$$q = \frac{\langle\phi|\hat{z}|g\rangle}{\pi V^* \langle E|\hat{z}|g\rangle}. \quad (3.7)$$

The reduced energy, ϵ is defined as $\epsilon = 2(E - E_\phi)/\Gamma$, where E_ϕ is the resonance energy and Γ is the width of the resonance. V^* describes the interaction between the bound and continuum states. The final state is modified with the resonance factor $R(\epsilon)$,

$$R(\epsilon) = \frac{q + \epsilon}{\epsilon + i}. \quad (3.8)$$

In Fig. 3.3 b) the amplitude (blue curve) and phase (red curve) of $R(\epsilon)$ is shown for the 2s2p Fano resonance in helium. This Fano resonance has $q = -2.77$. Around the resonance energy there is a phase jump of π radians. In Fig. 3.3 c) the complex trajectory of $R(\epsilon)$ is shown. At $\epsilon \rightarrow \pm\infty$, $R(\epsilon) = 1$. At $\epsilon = E_\phi$ the complex trajectory crosses the origin giving a π phase jump.

3.2 Reconstruction of attosecond beating by interference of two photon transitions (RABBIT)

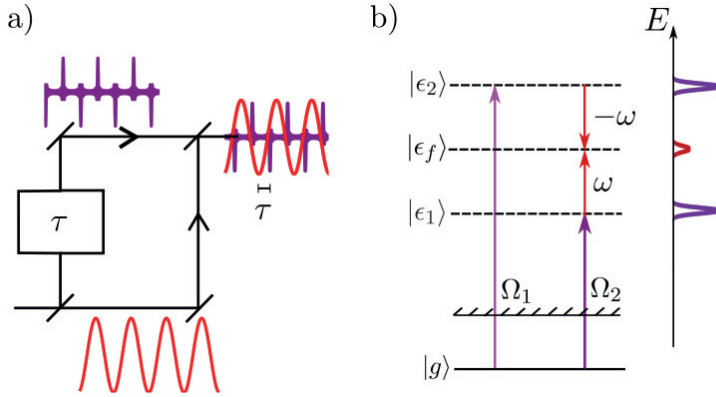


Figure 3.4: a) Optical Mach-Zehnder interferometer and b) photoelectron interferometer. RABBIT utilizes a Mach-Zehnder interferometer with an APT pump and IR probe with variable temporal delay. Ω_1, Ω_2 are the frequencies of two consecutive harmonics. $|\epsilon_1\rangle, |\epsilon_2\rangle$ are the states reached by absorption of XUV only radiation. $|\epsilon_f\rangle$ is reached by interfering two-photon transitions.

Reconstruction of Attosecond Beating By Interference of two photon Transitions (RABBIT) [4, 58, 59] is an attosecond photoelectron interferometry technique that uses an attosecond pulse train (APT) as pump, and a weak fraction of the generating IR field as the probe. The principle of RABBIT is shown in Fig. 3.4

a). In an interferometer (e.g. Mach-Zehnder), a combination of APT and IR probe at a variable time delay (τ) is prepared. Both beams are focused down in a gas jet where electrons are ionized. In Fig. 3.4 b) the electron spectrum obtained after absorption of the XUV field is shown in purple. The atom can additionally absorb or emit an IR photon, generating the sidebands shown in red. Since two paths end up at the same state $|\epsilon_f\rangle$, there is quantum interference. By scanning the pump-probe delay, the phase of the arms of the quantum interferometer is changed giving rise to sideband oscillations as $\sim \cos(2\omega\tau + \Delta\phi)$, where $\Delta\phi$ is the phase difference between the two paths.

Fig. 3.5 shows a RABBIT scan in helium. The phase of the sideband oscillation includes the spectral phase of the ionization process as well as the phase difference between consecutive harmonics.

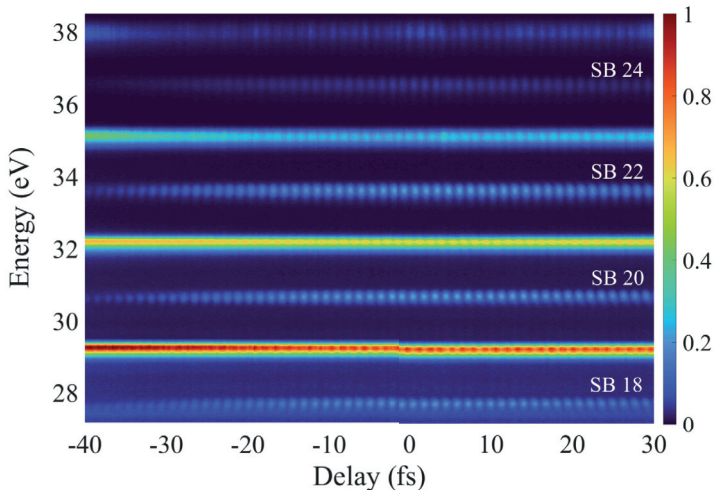


Figure 3.5: RABBIT scan in helium. Figure adapted from paper VII.

The RABBIT equation can be derived by using first order perturbation theory in quantum mechanics [60]. Here, since the density matrix will be used in chapter 4, we derive the RABBIT equations using the same formalism, for a single final scattering state. We do not consider the effect of several angular channel channels.

The signal at the final energy ϵ_f , is given as the population of the density matrix in the scattering state representation $\hat{\rho}_{\text{xuv+ir}}$,

$$S(\epsilon_f) = \langle \epsilon_f | \hat{\rho}_{\text{xuv+ir}} | \epsilon_f \rangle. \quad (3.9)$$

The interaction of the electron with the infrared probe field can be formally described as the action of a unitary operator on the density matrix due to absorption of the XUV photon $\hat{\rho}_{\text{xuv}}$ as,

$$\hat{\rho}_{\text{xuv}+\text{ir}} = \hat{U}^\dagger(\tau, \omega) \hat{\rho}_{\text{xuv}} \hat{U}(\tau, \omega), \quad (3.10)$$

where τ is the pump-probe delay and ω the angular frequency of the probe field. Furthermore, the probe field is assumed to be monochromatic. \hat{U} is the scattering operator.

In paper **VI** a derivation of the KRAKEN protocol is shown (see chapter 4). By following the same approach and interchanging the probe frequencies, $\omega_1 \rightarrow \omega$ and $\omega_2 \rightarrow -\omega$, in the KRAKEN derivation and considering both the absorption and emission path, the signal, $S(\epsilon_f, \tau, \omega)$, can be written in terms of $\hat{\rho}_{\text{xuv}}$ as,

$$\begin{aligned} S(\epsilon_f, \tau, \omega) \approx & |\mu_{\epsilon_f, \epsilon_1}|^2 \rho_{\text{xuv}}(\epsilon_1, \epsilon_1) + |\mu_{\epsilon_f, \epsilon_2}|^2 \rho_{\text{xuv}}(\epsilon_2, \epsilon_2) \\ & + e^{i\omega\tau} \mu_{\epsilon_f, \epsilon_1} \mu_{\epsilon_f, \epsilon_2}^* \rho_{\text{xuv}}(\epsilon_1, \epsilon_2) \\ & + e^{-i\omega\tau} \mu_{\epsilon_f, \epsilon_2} \mu_{\epsilon_f, \epsilon_1}^* \rho_{\text{xuv}}(\epsilon_2, \epsilon_1), \end{aligned}$$

where $\epsilon_i = \epsilon_f \pm \hbar\omega$, with (+) for absorption and (−) for emission and, $\mu_{\epsilon_f, \epsilon_i}$, is the continuum-continuum transition matrix element defined as, $\langle \epsilon_f | \hat{z} | \epsilon_i \rangle$. The interaction with the infrared probe gives access to off diagonal terms of the one photon density matrix. Rewriting using, $2\text{Re}(z) = z + z^*$ gives,

$$\begin{aligned} S(\epsilon_f, \omega, \tau) \approx & |\mu_{\epsilon_f, \epsilon_1}|^2 \rho_{\text{xuv}}(\epsilon_1, \epsilon_1) + |\mu_{\epsilon_f, \epsilon_2}|^2 \rho_{\text{xuv}}(\epsilon_2, \epsilon_2) \\ & + 2|\mu_{\epsilon_f, \epsilon_1}| |\mu_{\epsilon_f, \epsilon_1}| |\rho_{\text{xuv}}(\epsilon_1, \epsilon_2)| \cos(2\omega\tau + \Delta\phi). \end{aligned} \quad (3.11)$$

The phase difference between consecutive harmonics, $\Delta\phi$, is given by,

$$\Delta\phi = \text{Arg}(\mu_{\epsilon_f, \epsilon_2}) - \text{Arg}(\mu_{\epsilon_f, \epsilon_1}) + \text{Arg}(\rho_{\text{xuv}}(\epsilon_1, \epsilon_2)). \quad (3.12)$$

The first two terms are the measurement induced continuum-continuum phases, and their difference is,

$$\Delta\phi_{\text{cc}} = \text{Arg}(\mu_{\epsilon_f, \epsilon_f+\omega}) - \text{Arg}(\mu_{\epsilon_f, \epsilon_f-\omega}). \quad (3.13)$$

If the state of the photoelectron is mixed, RABBIT cannot characterize the state since it cannot be described as a wavefunction [61]. In the case of a pure state electron wavepacket (one angular channel, no spin-orbit splitting of the ion), $\text{Arg}(\rho_{\text{xuv}}(\epsilon_1, \epsilon_2))$, is the sum of the phase difference introduced from the group delay of the harmonics, denoted the attochirp and the scattering phase

difference,

$$\text{Arg}(\rho_{\text{xuv}}(\epsilon_1, \epsilon_2)) = \Delta\phi_{\text{xuv}} + \Delta\eta_L. \quad (3.14)$$

The Wigner delay can be approximated from the finite difference of the spectral derivative of the scattering phase as,

$$\tau^{\text{EWP}} = \hbar \frac{\partial \eta_L}{\partial E} = \hbar \frac{\Delta \eta_L}{\Delta E} + \mathcal{O}(\Delta E). \quad (3.15)$$

Since the energy spacing of two consecutive harmonics is $2\hbar\omega$, the Wigner time delay in first order approximation becomes,

$$\tau^{\text{EWP}} \approx \frac{\Delta \eta_L}{2\omega}. \quad (3.16)$$

The RABBIT technique has enabled the measurement of the Wigner time-delay [6, 62, 63] and the study of photoionization dynamics on its natural time scale. Broadband RABBIT has been used in papers **I**, **II**.

In papers **III**, **IV** and **V** we apply the energy resolved RABBIT or Rainbow RABBIT [10], where the spectral amplitude and phase is measured across a sideband. Eq. (3.11) is strictly speaking valid for monochromatic radiation. Finite pulse effects can be included by taking the convolution of the optical pump field, with the optical probe field multiplied with the two photon transition matrix element [64]. The finite bandwidth of the probe, in particular, limits the spectral resolution. Therefore some of the results in (papers **IV** and **V**) have been obtained with a reduced probe bandwidth.

By Fourier transformation of the spectral wavefunction the temporal wavefunction can be computed. Using the spectral or temporal wavefunction, it is possible to analyze the state of the photoelectron in the time-frequency domain. Examples of such time-frequency methods are, Gabor analysis [65], the Wigner function [52], and by construction of the build up of the EWP [10, 66]. The build-up of the EWP is given by,

$$\psi(\epsilon, \tau) = \int dt e^{i\epsilon t} \psi(t) \theta(t - \tau). \quad (3.17)$$

The build-up cuts the dynamics with a moving Heaviside function and by inverse Fourier transform the spectra for different times are obtained. From the build-up

the transient Wigner function can be calculated as,

$$W_f(\epsilon, t, \tau) = \int d\xi \, e^{i\xi t} \, \psi^\dagger\left(\epsilon - \frac{\xi}{2}, \tau\right) \psi\left(\epsilon + \frac{\xi}{2}, \tau\right). \quad (3.18)$$

Additionally, assuming pure state, the evolution of the density matrix of the EWP can be computed as,

$$\rho(\epsilon, \epsilon', \tau) = \psi^\dagger(\epsilon, \tau) \psi(\epsilon', \tau). \quad (3.19)$$

These time frequency analysis methods are useful for uncovering subtle structures in the photoionization dynamics.

3.3 Setup

As part of my PhD studies, the attosecond pump probe interferometer was redesigned and rebuilt. The new design has the same parity in the number of reflections in both interferometer arms, advantageous for passive beam-pointing stability. Finally, new vacuum chambers with better differential pumping and new optics were installed.

3.3.1 Attosecond photoelectron interferometer

Details on the attosecond photoelectron interferometer and its performances can be found in paper **VII**, below follows a brief description of the experimental setup.

In Fig. 3.6 a schematic of the Mach-Zehnder interferometer is presented. The pump beam is shown in red and the probe in yellow. Laser pulses at a repetition rate of 3 kHz and with a pulse energy up to 4 mJ, are generated in a Titanium-Sapphire CPA system with spectral bandwidth tunable in the range of 40-80 nm. The central wavelength can be varied between 790 and 810 nm. The laser tunability is advantageous when studying atomic resonances, since the central wavelength can be centered at the resonance energy. The laser is sent on a 40-60 beamsplitter that divides the pump beam and the probe beam with 40% of the intensity in the pump beam and 60% in the probe beam. The pump beam is first sent on a motorized delay stage with two mirrors in retro-reflective configuration.

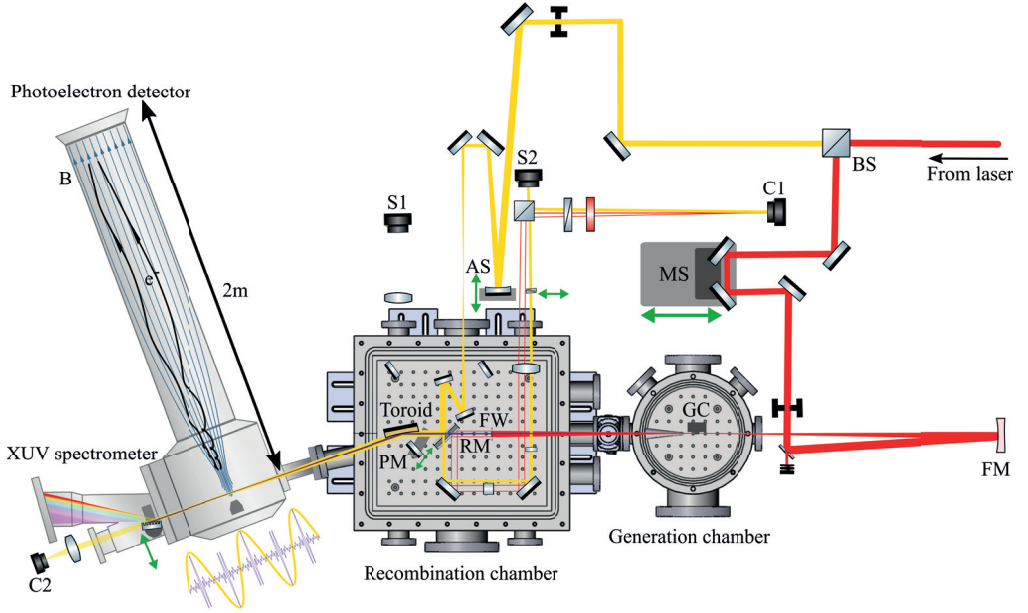


Figure 3.6: Schematic of the Mach-Zehnder attosecond photoelectron interferometer. The laser is incident on a 40-60 Beam Splitter (BS) that separates the pump and the probe. The pump is then sent on a Motorized Stage (MS) and focused down with a dielectric Focusing Mirror (FM) into the Gas Cell (GC). HHG is generated and transmitter through a metallic filter in a Filter Wheel (FW) recombined with the probe in a Recombination Mirror (RM). The pump probe delay is controlled with an Attosecond delay Stage (AS). A Pickup Mirror (PM) can be inserted to look for temporal overlap on the Spectrometer (S1). Figure adapted from paper VII.

This delay stage is used for coarse adjustments of the temporal delay between the pump and the probe beams and is usually used to find temporal overlap. The pump beam is then sent through an iris used for alignment, on a holey mirror that cuts the center of the beam. It is finally focused down by a dielectric concave spherical mirror with a focal length of 50 cm. The pump beam propagates through a sapphire window into the generation vacuum chamber with a pressure of 10^{-7} mbar and 10^{-3} mbar with gas load. The beam is focused in a 6 mm long pulsed gas cell supplied from Amsterdam Piezo Valve. The gas cell is mounted on a Smaract 2d linear translation stage that allows for translation of the gas cell in the xy -plane. Additionally there is a Newport stage mounted on the Smaract stage that allows for adjustment of the angle of incidence, in total giving motorized control of five degrees of freedom ($x, y, z, \theta_x, \theta_y$). In the gas

cell high-order harmonics are generated. The XUV radiation and the pump IR propagate colinearly into the recombination vacuum chamber with a pressure of 10^{-6} mbar. The central part of the pump IR is filtered out using a metallic foil filter mounted on a fused silica plate in a Smaract filter wheel. The outer part of the pump IR is not filtered by the metallic foil and later used for active temporal stabilization with the probe. The XUV radiation is then sent through a recombination mirror where it is overlapped with the probe IR and then focused down using a toroidal mirror (2f configuration with $f = 60$ cm) into an effusive gas jet in the Chamber for Atomic and Molecular Physics, (CAMP). Here the XUV radiation ionizes electrons, that are analyzed by an electron spectrometer, here a magnetic bottle spectrometer.

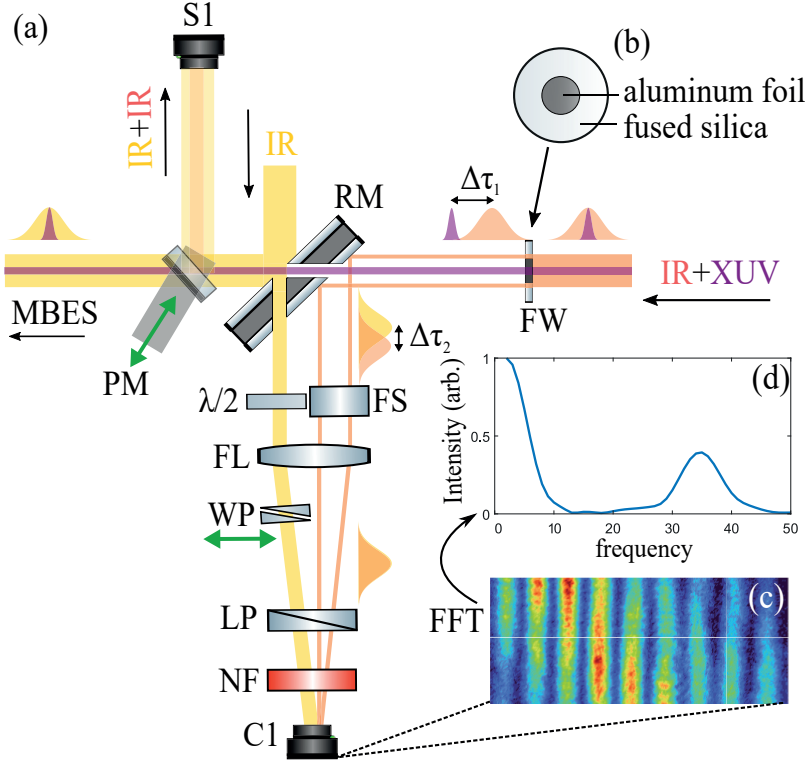


Figure 3.7: Schematic of the active stabilization loop. The outer part of the pump IR is transmitted through the fused silica plate and on the Recombination Mirror (RM) after which it is reflected and sent into a piece of Fused Silica (FS) and focused down with a Focusing Lens (FL) on a Linear Polarizer (LP) a Narrowband Filter (NF) and finally a Camera (C1). The probe IR is transmitted through the RM on a $\lambda/2$ -plate through the FL on tunable Wedge Pair (WP) and on the camera. Figure adapted from paper VII.

After the interaction region, both the APT and the IR probe are propagated

on a Hitachi concave grating that is mounted on a linear Smaract stage. The first diffraction order of the HHG is then imaged onto a MCP after which there is a phosphor screen with a camera imaging the screen, forming the XUV spectrometer. Using this design it is possible to measure the XUV spectra and the photoelectron spectra simultaneously. To overlap the pump and the probe field spatially, the grating can be moved out using the linear translation stage, sending the beam on a lens that focuses down the two beams on a camera.

In Fig. 3.7 a schematic of the active temporal stabilization loop is shown. High resolution RABBIT measurements require long term temporal stability between the XUV and IR pulses on the order of tens of as. To ensure temporal stability, an active stabilization loop is implemented. The outer part of the pump IR is reflected on the recombination mirror, delayed with a fused silica piece and focused down on camera. The probe IR is transmitted through a hole in the recombination mirror via a $\lambda/2$ -plate for contrast control and then focused down through a tunable wedge pair on the camera creating interference fringes. Both pulses are narrowband filtered with a 10 nm bandpass filter to ensure fringes for a long scan range (-400, 400) fs.

The stabilization procedure consists in first removing the aluminum filter by rotating the Smaract filter wheel, moving in the pick-up mirror (PM) and looking for spectral fringes on the spectrometer (S1) (Fig. 3.6). Here the motorized stage (MS) can be manually turned to find temporal overlap. The fringes on S1 estimates the temporal overlap between pump and probe in the interaction region in the CAMP, neglecting the transmission through the metallic filter. The filter can then be realigned and the pick-up removed. By tuning the dispersion in the wedge pair temporal overlap can be found on the camera which in turn can be actively stabilized using a feedback loop with error signal from the phase of the interference signal of the FFT. The feedback loop then actuates the attosecond delay stage (AS).

3.3.2 Electron spectrometers

For the experiments conducted, two types of spectrometer are used. In Fig. 3.8, a schematic of the Magnetic Bottle Electron Spectrometer (MBES) and the Velocity Map Imaging (VMI) is shown.

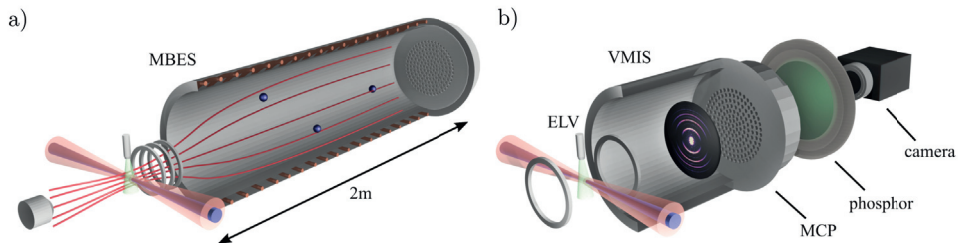


Figure 3.8: Schematic of the MBES a) and the VMI b). The MBES are used as the photoelectron detector in papers **I**, **II**, **III**, **IV**, **V** and **VIII**, while the VMI is used in paper **III**. Figure adapted from paper **III**.

By default, the MBES is used thanks to its high spectral resolution and transmission. In the MBES, electrons are guided by a magnetic field from a permanent magnet into a drift tube to a detector. The electrons are subject to cyclotron motion and from the time of flight it is possible to calculate the kinetic energy of the electrons at ionization. For the MBES the conversion between time-of-flight time and photoelectron kinetic energy is given by,

$$E = \frac{m_e(L + \gamma)^2}{2t_{\text{tof}}^2}, \quad (3.20)$$

where m_e is the electron mass, L the length of the flight tube, t_{tof} the time it takes for the electron to reach the detector and γ a calibration parameter. As can be seen in Eq. (3.20) the resolution of the spectrometer scales proportional to the length of the magnetic bottle, therefore it is advantageous to have a long bottle. For this work, a bottle of length 2 m is used. In the flight tube, the electron is assumed to propagate classically with constant kinetic energy. The electron collides with the multi-channel plate (MCP) at the end of the drift tube initiating an electronic cascade that is then detected. It is possible to apply a voltage in the magnetic bottle to decelerate electrons down to 1-2 eV where the MBES has the highest resolution, $\Delta E/E \approx 2\%$.

For the measurements in paper **III**, a VMI allowing for angular resolution is used to study resonant two-photo ionization in helium. In the VMI electrons are focused with an electrostatic lens onto a MCP after which there is a phosphor screen that is imaged by a camera. At the MCP the photoelectron angular distribution (PAD) is projected on a plane. Using Abel inversion it is possible, from the 2d projection, to reconstruct the PAD. The resolution of a VMI scales as, $\Delta E/E \approx 5\%$, giving a lower spectral resolution than that of the MBES.

3.4 Resolution

The spectral measurement of the electron with a MBES can be mathematically formulated as the convolution between the MBES point-spread function (PSF) and the kinetic energy spectrum (S_{raw}) of the electron.

$$S_{\text{measured}}(\epsilon) = \int d\epsilon' \text{psf}(\epsilon') S_{\text{raw}}(\epsilon - \epsilon') \quad (3.21)$$

The PSF limits the spectral resolution of the MBES. The PSF is a consequence of volume averaging in the interaction region of the CAMP and the angular integration. It is possible to remove the convolution by use of spectral deconvolution. Spectral deconvolution is implemented in paper **V** using blind Richardson-Lucy deconvolution [67, 68].

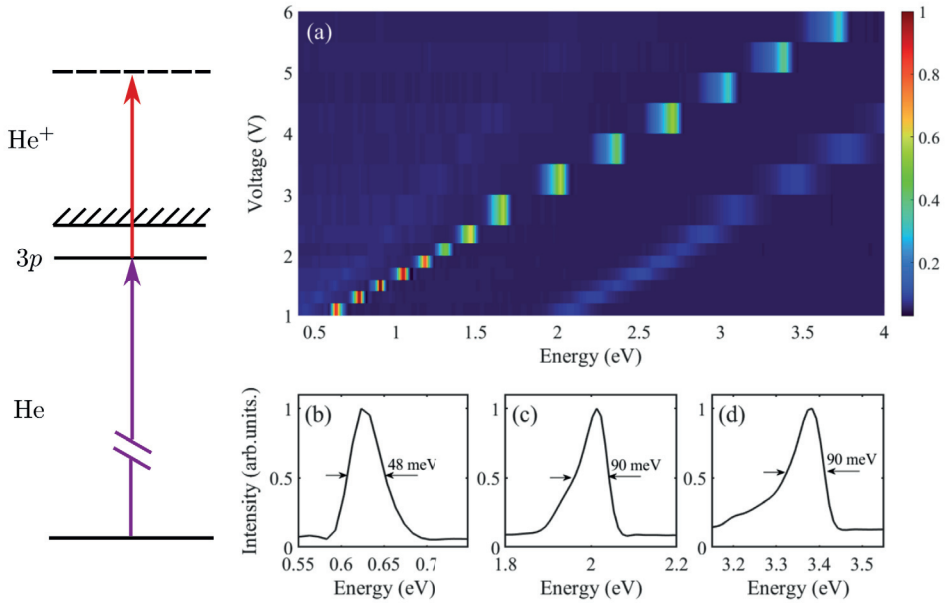


Figure 3.9: Characterization of the spectral resolution of the MBES by below threshold ionization of the helium 3p state and varying the retarding potential.

In Fig. 3.9 the kinetic energy spectra measured with the MBES of a resonant two-photon process is shown for different retarding potentials. A spectrally

broad harmonic excites the $3p$ Rydberg state in helium and an electron is ionized through the absorption of a secondary narrow-band filtered (10 nm) IR photon. The width of the electron peak is given as the convolution of the resonance width with the IR field and the point spread function of the MBES. The width of the electron peak is to a good approximation given as the MBES point spread function. The point spread function broadens for increasing kinetic energy and by scanning the retarding potential the point spread function as function of kinetic energy can be determined. To maximize spectral resolution in rainbow RABBIT the retarding potential is applied such that the kinetic energy of the photoelectron is around 1 eV. Here the resolution of the spectrometer is < 50 meV.

3.5 Results I: Time-delays

In this section broadband attosecond time-delay measurements are presented using RABBIT to study subtle aspects of electron correlation, such as the $3s$ and $3p$ Cooper minimum in argon and the Giant dipole resonance in xenon.

3.5.1 Paper I: Attosecond photoionization dynamics in the vicinity of the Cooper minima in argon

In this work the Rainbow RABBIT technique is used to measure the photoionization time-delay difference between the $3s$ and $3p$ subshells in a large spectral range, ~ 34 eV, covering both the $3s$ and the $3p$ Cooper minima. The Cooper minimum is an interesting phenomenon caused by the zero crossing of the $3p \rightarrow \epsilon d$ radial transition matrix element. Due to electron correlation, the $3p$ Cooper minima is imprinted in the $3s$ ionization channel. The Cooper minimum is reflected in the ionization cross section as a sharp decrease.

In the following, we call $3p$ ($3s$) harmonics the electron peak due to absorption of one harmonic from the $3p$ ($3s$) state and $3p$ ($3s$) sidebands the electron peak following a two-photon transition from the $3p$ ($3s$) state. Different contributions may partially overlap spectrally. Using Rainbow RABBIT, with high spectral resolution, it is possible to disentangle processes due to absorption of one harmonic from the $3p$ state and the sideband following a two-photon transition from the $3s$ state.

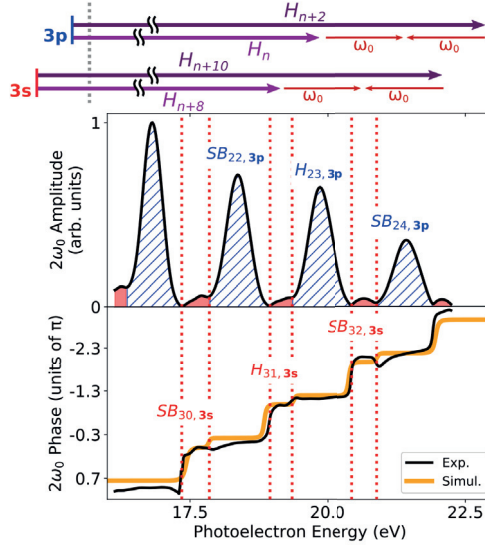


Figure 3.10: 2ω amplitude (top panel) and phase (bottom panel) retrieved from Rainbow RABBIT measurements across the $3s$ - $3p$ Cooper minima in argon performed in Saclay. H_n denotes the n th harmonic. $H_{n,3s}$ ($H_{n,3p}$) denotes the electron peak due to absorption of the n th harmonic from the $3s$ ($3p$) state. $SB_{n\pm 1,s}$ ($SB_{n\pm 1,p}$) denotes the electron peak following a two-photon transition from the $3s$ ($3p$) state. Figure adapted from paper I.

In Fig. 3.10 the retrieved amplitude of the oscillations with frequency 2ω (top panel), and phase (bottom panel) are shown. The red regions in the top panel correspond to $3s$ harmonics and sidebands, while the blue peaks correspond to $3p$ harmonics and sidebands. In the bottom panel the black curve shows the retrieved phase and the yellow curve the phase from theoretical calculations. As can be seen there is a spectral overlap between $3p$ harmonics and $3s$ sidebands. However it is possible to retrieve the $3p$ and $3s$ sideband phases despite the partial spectral overlap with the harmonics, by taking the phase value from spectral regions without overlap. The cross section for $3s$ ionization is about one order of magnitude lower than the $3p$ ionization cross section. This results in one order of magnitude difference in the signal-to-noise ratio between $3s$ and $3p$ phases, making it challenging to retrieve the $3s$ phase.

In Fig. 3.11 the Wigner-time delay difference between the $3s$ and $3p$ shells in argon is shown. The purple points are from measurements by us while the yellow points are from measurements of the Saclay group. The green curve shows the delay difference calculated using the Two-Photon Two-Color Random Phase Approximation with Exchange. In general there is good agreement

between measurement and theory, however not in the region around the 3s Cooper minimum. This discrepancy between theory and experiment is attributed to overlapping contributions of shake-up states. The large phase retrieval error close to the 3s Cooper minimum is caused by the low 3s ionization cross section going to zero at the Cooper minimum.

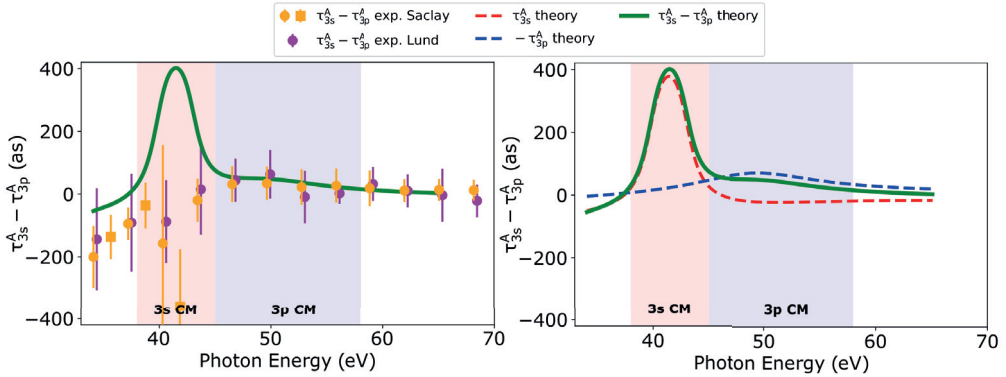


Figure 3.11: Time-delay measurements across the 3p and 3s Cooper minima in argon. Figure adapted from paper I.

3.5.2 Paper II: Attosecond electron-spin dynamics in xenon 4d photoionization

Another interesting case of electron correlation is photoionization in the region of the Xe 4d giant dipole resonance, which has been a subject of study for many years [23, 24]. The resonance is very broad and a consequence of collective many-electron effects in the 4d shell.

In Fig. 3.12 (a) a schematic of the photoionization process is presented. A XUV photon ionizes an electron from the 4d shell. This process is followed by Auger decay. For example, a 5s electron fills the hole in the 4d shell and a 5p electron is emitted. The energy diagram in Fig. 3.12 (b) shows the intermediate and final states of the ion. The spin-orbit interaction in leads to a splitting of 2 eV for the $4d^{-1} {}^2D_{5/2}$ and ${}^2D_{3/2}$ states of the Xe^+ ion.

In these measurements RABBIT is combined with coincidence spectroscopy to disentangle spectrally overlapping electron peaks [69]. In Fig. 3.13 a two-electron coincidence map is shown. The electron emitted from the 4d shell is referred to as the fast electron and the electron emitted from the $n = 5$ shell the slow electron. This notation is due to the kinetic energy difference between

the $4d$ photoelectron and the Auger electron, emitted from the $n = 5$ shell.

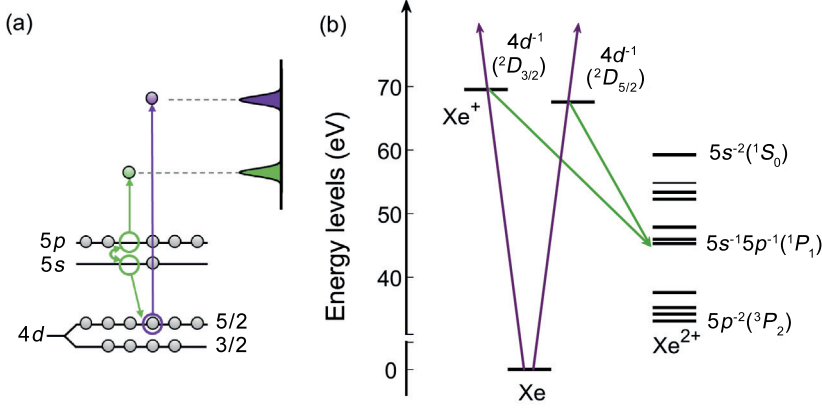


Figure 3.12: (a) Schematic illustration of Xe $4d$ direct photoionization (purple) and Auger decay processes (green) after absorption of a XUV photon. (b) Xe energy diagram showing the Xe^+ intermediate and Xe^{2+} final states involved. Figure adapted from paper II.

For coincidence measurements we limit the ionization rate to one event per laser shot, such that we can correlate the kinetic energy of the fast electron with the slow electron. This requires a long measurement time, making the experiment challenging. Fig. 3.13 shows the measured photoelectron coincidence map with XUV-only (a) and XUV + IR (b). By fitting the sideband oscillations, the phases can be extracted. While the variation of the phase with energy determines the time delay, the comparison of the phases from the same sideband order, for different ionic cores informs on the influence of the spin-orbit coupling in photoionization. The phases are found to be independent of the subsequent Auger decay.

We measure a 100 as time delay difference between Xe $4d_{5/2}$ and Xe $4d_{3/2}$ near the $4d$ threshold. With theoretical calculations, using the Relativistic Random Phase Approximation (RRPA) method, we show that the measured 100 as time delay is a consequence of interference due to several resonances. The spin-orbit coupling in Xe weakens the dominating role of LS-coupling in the near threshold region, giving rise to the LS-forbidden transition from singlet ground state to triplet $4d^9 f^3 P$ and $^3 D$ states. The drastic variation in the photoionization time delay can be attributed to the mixing of singlet and triplet resonances in this region.

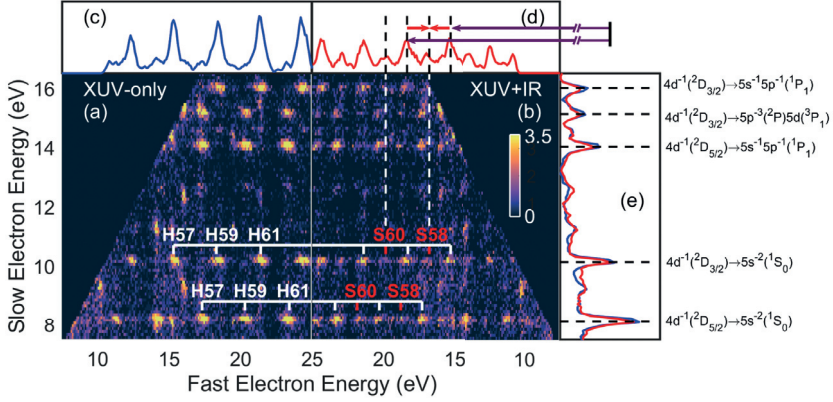


Figure 3.13: Two-electron coincidence spectra using (a) XUV only and (b) XUV+IR. The projection on the slow electron energy axis (e) shows Auger electron peaks labelled with the corresponding decay. Spots with a fixed slow electron energy and different fast electron energies indicate the energy of the photoelectron detected in coincidence with the Auger electron (labelled e.g. as H57-H61 in (a)). The projection on the fast electron energy axis (c) and (d) is a cut for the photoelectrons in coincidence with $4d^{-1}(^2D_{3/2}) \rightarrow 5s^{-2}(^1S_0)$ Auger electrons. In (d), the sidebands arising from the two-photon transition can be observed (labelled e.g. as S58 and S60 in (b) in contrast to the previous convention). Figure adapted from paper II.

3.6 Results II: Resonances

In this section paper III, IV and V are summarized, more details about the results are found in the respective articles.

3.6.1 Paper III: Resonant two-photon ionization of helium atoms studied by attosecond interferometry

In this work we study two-photon ionization of He via the below threshold $1s3p$, $1s4p$, and $1s5p$ resonances using the rainbow RABBIT technique. We measure the photoelectron spectral amplitude and phase across the $1s3p$, $1s4p$ and $1s5p$ states using both a velocity map imaging spectrometer and a magnetic bottle electron spectrometer.

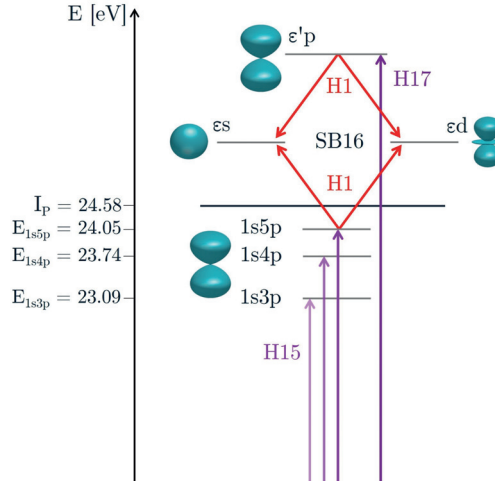


Figure 3.14: Energy diagram of the $1s3p$, $1s4p$ and $1s5p$ below threshold resonances in helium. In purple the XUV transitions are shown and in red the IR transitions. In sideband 16, (SB_{16}), the PAD is a superposition of s and d partial waves. Figure adapted from paper III.

In Fig. 3.14 the energy diagram of the processes involved are shown. Harmonic 15 can be tuned to promote a $1s$ electron to the $3p$, $4p$ or $5p$ atomic orbitals. By absorption of an IR photon the electron is subsequently ionized. The resonant excitation, via a discrete state, leads to a rapidly varying phase of the photoelectrons as function of kinetic energy and emission angle.

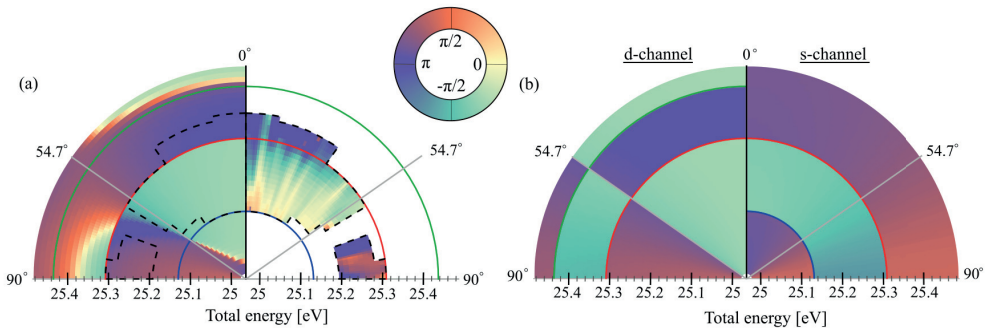


Figure 3.15: Angle and energy resolved phase of sideband 16, across the $4p$ resonance. (a) Left panel shows theoretical phase obtained from two-photon RRPA calculations, while the right panel show measured phase. In (b) left panel the contribution to the total phase from the d -channel is shown while in the right the contribution from the s -channel. Figure adapted from paper III.

In Fig. 3.15 (a,right) the measured phase of the 2ω component of the photoelectron angular distribution (PAD) obtained using the VMI spectrometer is shown. The red semi-circle indicates the resonance energy of the $4p$ resonance. The white areas correspond to spectral regions where it was not possible to retrieve the phase of the oscillations (too low signal to noise ratio). Comparing the measured phase to the theoretical (a,left), there is great similarity. In Fig. 3.15 (b,left) and (b,right) the theoretical phase is decomposed into the d - and the s -channel. The total phase in Fig. 3.15 (a,left) is similar to 3.15 (b,left) indicating that the resonant path to the d -wave dominates. However at the magic angle 54.7° , the d -wave vanishes because the spherical harmonic $Y_{2,0}$ is zero and the s -channel dominates.

Angle resolved measurements can provide insight into the relative strength of the different partial waves and, in principle, enables the complete characterization of the electron wavepacket. With a VMI, through the measurement of the PAD, the momentum of the photoelectron is reconstructed. Using a MBES, the emission angle is integrated over, yielding the kinetic energy as the observable, with higher spectral resolution than what is possible with a VMI. The lower spectral resolution as compared to angle integrated measurements make these measurements challenging. Through these measurements we could give a complete characterization of the resonant electron wavepacket (phase and amplitude) in emission angle and energy.

3.6.2 Paper IV: Breaking time reversal symmetry of Fano resonances in attosecond photoelectron interferometry

In this work the $3s^{-1}4p$ Fano resonance in argon is studied using Rainbow RABBIT. This particular resonance has been studied previously in Lund [8, 51]. The objectives of revisiting this Fano resonance was to test the influence of the improved spectral resolution and temporal stability with our upgraded setup (chapter 4 and paper VII). In the case of argon, the spin orbit splitting energy is $\epsilon_{\text{SO}} = 177$ meV. Due to the spin-orbit splitting, the one photon wavepacket has two copies, one for $j = 1/2$ and one for $j = 3/2$. Since the states of the ion are orthogonal, the electron spectrum is the incoherent sum of the individual spectra corresponding to the two spin-orbit components, which can be approximately described by the same distribution, with a difference of a factor 2 in amplitude and a shift of energy by ϵ_{SO} ,

$$S_{\text{electron}}(\epsilon) = \frac{1}{3}S_{\text{Fano}}(\epsilon) + \frac{2}{3}S_{\text{Fano}}(\epsilon - \epsilon_{\text{SO}}). \quad (3.22)$$

The $3s^{-1}4p$ resonance is a window resonance, with a q -parameter equal to -0.25 . In the previous measurement [51], the destructive interference from the Fano resonance was not visible in the amplitude and the spin-orbit components were not well resolved. Now with improved spectral resolution we can see both the spin-orbit splitting and the window resonance in the two spin-orbit components.

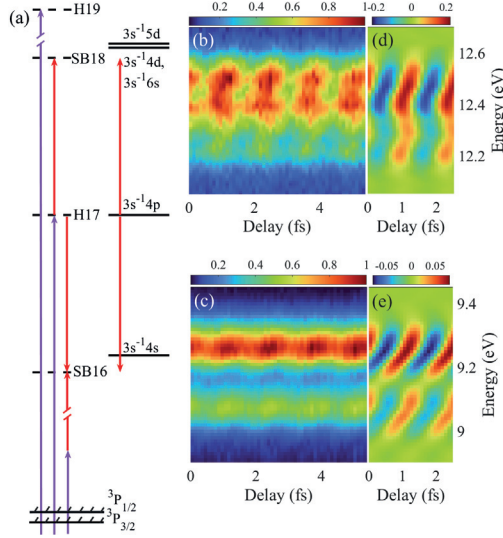


Figure 3.16: (a) Energy diagram for the $3s^{-1}4p$ Fano resonance in argon. (b,c) Sideband oscillations for SB (18,16) respectively. (d,e) shows the 2ω Fourier filtered SB oscillations. Figure adapted from paper IV.

In Fig. 3.16 (a) the energy diagram of the processes involved in our measurement is shown. H_{17} is tuned to be resonant with the $3s^{-1}4p$ state. In Fig. 3.16 (b,c) the sideband oscillations are shown as function of delay for SB₁₈ and SB₁₆. There is a strong asymmetry between SB₁₆ and SB₁₈, which are even more visible in (d) and (e) with scans filtered at the 2ω component.

In Fig. 3.17(a,b) the 2ω amplitude and phase are shown for SB₁₆ and SB₁₈ respectively. In SB₁₆ The phase variation across the resonance is 4 rad while only 1 rad in SB₁₈. This huge phase difference cannot be explained using the 1-photon matrix element for the Fano resonance which only allows for a maximal phase variation of π . Therefore a model including the IR probe field as weak perturbation was developed to explain the large phase variation.

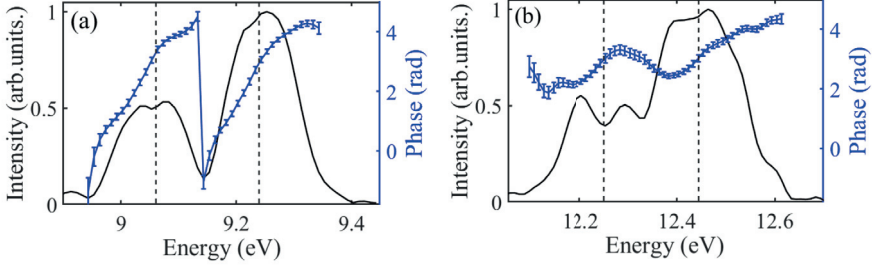


Figure 3.17: (a,b) Shows the retrieved amplitude and phase for SB_{16} and SB_{18} . Figure adapted from paper IV.

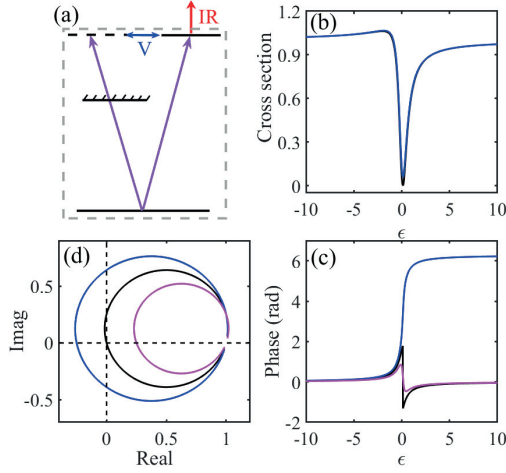


Figure 3.18: (a) Energy diagram of the Fano resonance assuming a single continua. (b) Cross section, (c) phase, and (d) complex trajectory of the Fano resonance for different values of the q -parameter. Figure adapted from paper IV.

In Fig. 3.18(a) the energy diagram of a Fano resonance is shown assuming a single quasi-bound state and a single continuum. The IR probe is included in the diagram as it can through absorption or stimulated emission of an infrared photon from the $3s^{-1}4p$ state followed by autoionization lead to a broadening of the discrete state. This broadening is included by allowing the resonance energy to become complex, $E_r \rightarrow \bar{E}_r + i\gamma$. Inserting the complex resonance energy in the expression for the 1-photon resonance factor, $R(\epsilon)$, and performing algebraic manipulation it can be shown that this corresponds to a complexification of the q -parameter,

$$q \rightarrow q \mp 2(q - i)\gamma/\Gamma, \quad (3.23)$$

where the \mp is $+$ for absorption to SB_{18} and $-$ for emission to SB_{16} . In Fig. 3.18(d) the complex trajectory of the resonance factor $R(\epsilon)$ is shown for three different q -parameters, $q = -0.25$ (black), $q = -0.25 - 0.25i$ (blue) and $q = -0.25 + 0.25i$ (pink). In Fig. 3.18(c) and (d) the argument and phase of $R(\epsilon)$ are shown. When the origin is inside the complex trajectory, the argument of $R(\epsilon)$ has a 2π phase jump, while when the origin is outside, the phase jump is smaller than π . This explains the strong differences between SB_{16} and SB_{18} since the sign change of the imaginary addition to the q -parameter is different for absorption and emission. Additionally the measurement of a complex q -parameter implies that time-reversal symmetry is broken for the system indicated inside the dashed rectangle in Fig. 3.18(a), due to a portion of the population of the $3s^{-1}4p$ being dissipated from the quantum interferometer made of the Fano resonance.

3.6.3 Paper V: Probing electronic decoherence with high-resolution attosecond photoelectron interferometry

This study examines the ionization dynamics of the $2s2p$ resonance in helium using attosecond interferometry with high spectral resolution, while keeping a temporal resolution down to the attosecond time scale. This enables us to calculate the time-dependent Wigner representation and to perform a quantum state reconstruction of the ionizing EWP. We use the energy resolved RABBIT technique (Rainbow-RABBIT) [10] with a narrow band probe pulse (10 nm). The spectral resolution is limited by the magnetic bottle spectrometer (MBES) response width of 90 meV. A blind Richardson-Lucy deconvolution algorithm is used to compensate for the point spread function of the MBES, increasing the spectral resolution to be close to the Heisenberg limit. The RABBIT technique allows both the spectral phase and amplitude of the autoionized EWP to be measured from which the temporal profile of the EWP can be reconstructed.

In Fig. 3.19 (a,b) the retrieved amplitude and phase (blue) in SB_{38} is shown. The calculation (red curve) is based on a model assuming the EWP to be pure and fits the data well. We can therefore, under the pure state assumption, reconstruct the Wigner function. It is shown in Fig. 3.19 (e). Close to $t = 0$ the broad spectral feature corresponds to direct ionization while the long and spectrally narrow decay around 58.6 eV corresponds to autoionization. The fringes correspond to quantum interference between direct ionization and autoionization.

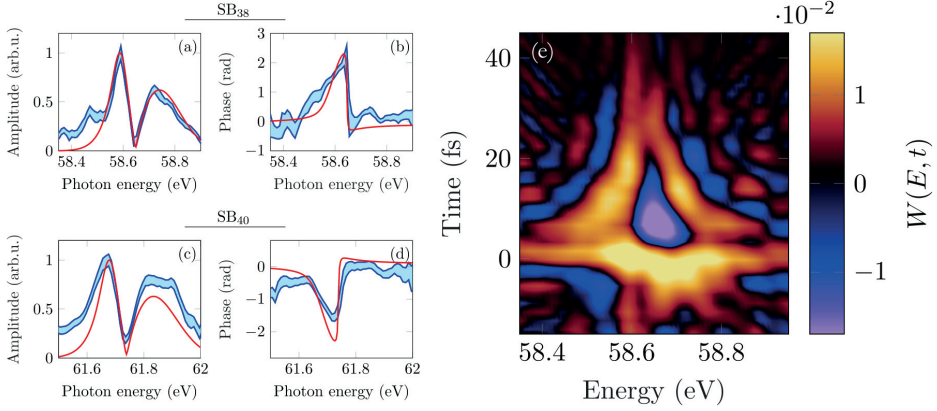


Figure 3.19: Spectral amplitude (a) and phase (b) retrieved in SB₃₈. Red curves are fits assuming pure state. In (c) The Wigner distribution of the spectral wavefunction in SB₃₈ is shown. Figure adapted from paper **V**.

For SB₄₀ the situation is slightly different. The calculation assuming a pure state (red curve) does not fit the data as well as for SB₃₈ [see Fig. 3.19 (c,d)]. The contrast is worse and the phase jump smaller, implying decoherence. We explain this result by considering the final continua ϵ_s , ϵ_d after two-photon ionization. The density matrix of the photoelectron can be expressed as,

$$\begin{aligned}
 \hat{\rho}_{\text{electron}}(t) &= |\psi_{\text{electron}}(t)\rangle \langle \psi_{\text{electron}}(t)| \\
 &= \int d\epsilon d\epsilon' \left(c_s(\epsilon, t) c_s^*(\epsilon', t) |R_s(\epsilon)\rangle \otimes |Y_{00}\rangle \langle R_s(\epsilon')| \otimes \langle Y_{00}| \right. \\
 &\quad + c_d(\epsilon, t) c_d^*(\epsilon', t) |R_d(\epsilon)\rangle \otimes |Y_{20}\rangle \langle R_d(\epsilon')| \otimes \langle Y_{20}| \\
 &\quad + c_s(\epsilon, t) c_d^*(\epsilon', t) |R_s(\epsilon)\rangle \otimes |Y_{00}\rangle \langle R_d(\epsilon')| \otimes \langle Y_{20}| \\
 &\quad \left. + c_d(\epsilon, t) c_s^*(\epsilon', t) |R_d(\epsilon)\rangle \otimes |Y_{20}\rangle \langle R_s(\epsilon')| \otimes \langle Y_{00}| \right) e^{\frac{i(\epsilon - \epsilon')t}{\hbar}},
 \end{aligned}$$

where, $R_l(\epsilon)$ is the radial amplitude for the angular momentum l and Y_{lm} the spherical harmonics. The MBES detects the photoelectrons independently of their emission angle, only their energy is determined. Therefore the angular degrees of freedom need to be traced over to obtain the measured EWP, char-

acterized by the radial density matrix,

$$\begin{aligned}
\hat{\rho}_{\text{radial}}(t) &= \text{tr}_{\theta,\phi}(\hat{\rho}_{\text{electron}}(t)) \\
&= \int d\epsilon d\epsilon' \left(c_s(\epsilon, t) c_s^*(\epsilon', t) |R_s(\epsilon)\rangle \langle R_s(\epsilon')| \right. \\
&\quad \left. + c_d(\epsilon, t) c_d^*(\epsilon', t) |R_d(\epsilon)\rangle \langle R_d(\epsilon')| \right) e^{\frac{i(\epsilon - \epsilon')t}{\hbar}}.
\end{aligned} \tag{3.24}$$

The radial density matrix of the photoelectron is the sum of the density matrices for the radial s and d continua. If $c_s(\epsilon, t) |R_s(\epsilon)\rangle \neq c_d(\epsilon, t) |R_d(\epsilon)\rangle$, the purity of the photoelectron is less than one and the photoelectron is described as a mixed state. For SB₄₀ this is the case as the $2p^2$ state, which is close to one IR photon above the $2s2p$ resonance, is of symmetry 1S_0 and can only couple to the s -channel yielding different spectral phase and amplitude for the s and d wavepackets.

As described in more details in paper V, the evolution of the s and d radial wavefunction can be calculated separately, the evolution of the mixed state density matrix can be reconstructed, and the purity can be calculated as function of time as, $\gamma(t) = \text{tr}(\hat{\rho}_{\text{radial}}(t))$.

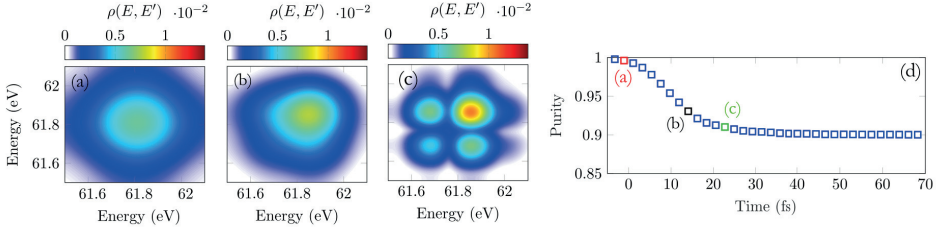


Figure 3.20: Evolution of density matrix in SB₄₀ (a,b,c) and purity (d). Off-diagonal elements represent coherences while the main diagonal represents the populations. (a,b,c) show the density matrix at different times (0, 12, 22) fs. In (a) only the direct path is visible since the EWP has not autoionized from the quasi-boundstate. At intermediate times (b), the coherences of the EWP show interference between the direct and autoionizing path. In (c) the coherences are more localized, clearly showing the destructive interference of the Fano resonance. Figure adapted from paper V.

Fig. 3.20 shows the evolution of the density matrix retrieved from SB₄₀. At $t = 0$, as shown in detail in paper V, only direct ionization takes place meaning that the state of the photoelectron is pure. As the $2s2p$ state gets excited and the s continuum is influenced by the $2p^2$ 1S_0 state the purity decreases to the

asymptotic value of 0.89.

It is challenging to quantify decoherence of EWP's using RABBIT since it employs a wavefunction formalism. Instead the density matrix should be measured directly using Quantum State Tomography (QST). In the next chapter a quantum state tomography protocol for photoelectrons ionized using attosecond pulses is presented.

Chapter 4

Quantum state tomography and decoherence in photoionization

4.1 Introduction

The gold standard for characterization of a quantum state is quantum state tomography. Quantum state tomography (QST) is the process of reconstructing the density matrix of an arbitrary quantum state. QST is performed through a sequence of projective measurements on the prepared state, from which the density matrix can be reconstructed. An analogy can be made with 3D tomography where a three dimensional geometry is to be determined by performing a sequence of planar projections. The planar projections have a dimension of one order less than the geometry that is to be characterized. The same holds for QST. In QST the density matrix is the higher dimensional object and through projective measurements the density matrix can be reconstructed.

There are density matrix reconstruction techniques for bound states using multidimensional spectroscopy [70–72]. 2D IR spectroscopy utilizes a pump pulse and two probe pulses with a variable delay between the probe pulses and a secondary variable delay between the pump and probe pulses. By scanning both delays and taking the Fourier transform, the coherence map can be built up from which the density matrix can be reconstructed. This approach does not work for continuum states, since the EWP is not bound to the interaction region and after the ionization moment, it will propagate away. Therefore an alternative

approach to project the density matrix of the EWP was implemented in the protocol developed in this thesis called KRAKEN.

In, [18, 21], quantum state tomography protocols for photoelectrons ionized with attosecond pulses are presented. In [18], the density matrix of an attosecond pulse train is reconstructed from which the purity of the pulse train is obtained. The density matrix of an electronic attosecond pulse train in the context of electron microscopy is reconstructed in [21].

4.2 KRAKEN

Kvantillståndstomografi Av attosekundElektroNvågpaket (KRAKEN), (Quantum state tomography of attosecond electron wavepackets), is an attosecond photoelectron interferometry protocol that utilizes a femtosecond XUV pump to ionize an EWP that is then probed with a bichromatic probe.

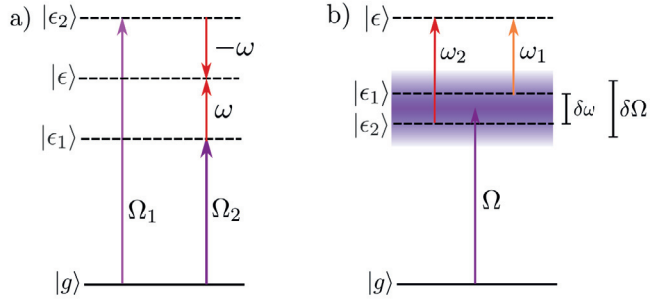


Figure 4.1: Energy diagram for RABBIT a) and KRAKEN b). RABBIT measures the degree of coherence of electron wave packets originating from absorption of consecutive harmonics by interfering H_{2q+1} with H_{2q-1} while KRAKEN measures the degree of coherence of an electron wave packet originating from absorption of a single harmonic by interfering the harmonic H_{2q+1} with itself.

In Fig. 4.1 the energy diagrams for RABBIT and KRAKEN are compared. In RABBIT two quantum paths involving absorption of consecutive harmonics interfere, while in KRAKEN different parts of the wavepacket due to absorption of one photon absorb different probe photons to interfere with each other.

The KRAKEN derivation is shown in detail in paper VI. Here we summarize the results. In KRAKEN, we only consider the absorption path from a harmonic and the probe field is bichromatic instead of monochromatic. We can write the

photoelectron spectrum due to absorption of XUV radiation (frequency Ω) and bichromatic field (frequencies ω_1 and ω_2) as,

$$\begin{aligned}
S(\epsilon_f, \tau, \delta\omega) \approx & |\mu_{\epsilon_f, \epsilon_1}|^2 \rho_{\text{XUV}}(\epsilon_1, \epsilon_1) + |\mu_{\epsilon_f, \epsilon_2}|^2 \rho_{\text{XUV}}(\epsilon_2, \epsilon_2) \\
& + e^{i\delta\omega\tau} \mu_{\epsilon_f, \epsilon_1} \mu_{\epsilon_f, \epsilon_2}^* \rho_{\text{XUV}}(\epsilon_1, \epsilon_2) \\
& + e^{-i\delta\omega\tau} \mu_{\epsilon_f, \epsilon_2} \mu_{\epsilon_f, \epsilon_1}^* \rho_{\text{XUV}}(\epsilon_2, \epsilon_1).
\end{aligned} \tag{4.1}$$

Here $\epsilon_i = \epsilon_f - \omega_i$ and τ is the delay between the XUV field and the bichromatic probe. Assuming that the continuum-continuum matrix elements, $\mu_{\epsilon_1, \epsilon_2}$, are constant¹, and taking the Fourier transform of the obtained photoelectron spectrogram along the delay, τ , for each energy bin and isolating the component oscillating at frequency $\delta\omega = \omega_1 - \omega_2$, one retrieves a signal that is proportional to the subdiagonal of the one-photon density matrix,

$$\mathcal{F}\{S(\epsilon_f, \tau, \delta\omega)\}(\delta\omega) \approx \mu_{\epsilon_f, \epsilon_1} \mu_{\epsilon_f, \epsilon_2}^* \rho_{\text{XUV}}(\epsilon_1, \epsilon_2). \tag{4.2}$$

By measuring a sequence of delay scans with different spectral components of the probe, ω_1 and ω_2 , the density matrix can be reconstructed.

In Fig. 4.2 a visualization of the reconstruction procedure of the KRAKEN protocol is shown, using simulations in He close to the $2s2p$ Fano resonance. First a pump-probe delay scan is computed with a single XUV harmonic as the pump and the bichromatic IR field as the probe. The delay needs to be scanned in a large range, spanning a number of beating periods ($\tau_{\text{beating}} \sim \hbar/\delta\omega$).

The delay scan is Fourier transformed over delay giving a Fourier map that has three peaks. The populations correspond to the DC component of the Fourier map, (first two terms in eq. (4.1)). The second contribution (positive frequency) is the subdiagonal of the density matrix at the interference frequency, $\delta\omega$, (third term in eq. (4.1)). The third peak is the fourth term in eq. (4.1) and therefore the complex conjugate of the second one. By selecting the row corresponding to the interference frequency and placing it in a matrix as indicated in the Fig. 4.2, a subdiagonal of the density matrix is reconstructed. The procedure is then repeated for different values of $\delta\omega$ and the sparse density matrix is reconstructed. Through interpolation of the sparse density matrix the continuous variable density matrix is reconstructed as shown in Fig. 4.2 d).

The main diagonal of the density matrix contains the populations, while the off-diagonal elements are the coherences, which encode the degree of coherence

¹This is a good approximation across the bandwidth of a harmonic in non-resonant conditions.

between continuum states. As a density matrix is subject to decoherence the coherences decay and the populations are left, yielding the maximally mixed state. Additionally the density matrix is normalized such that the populations sum up to 1, $\text{tr}(\rho) = 1$, for the preservation of the Born rule.

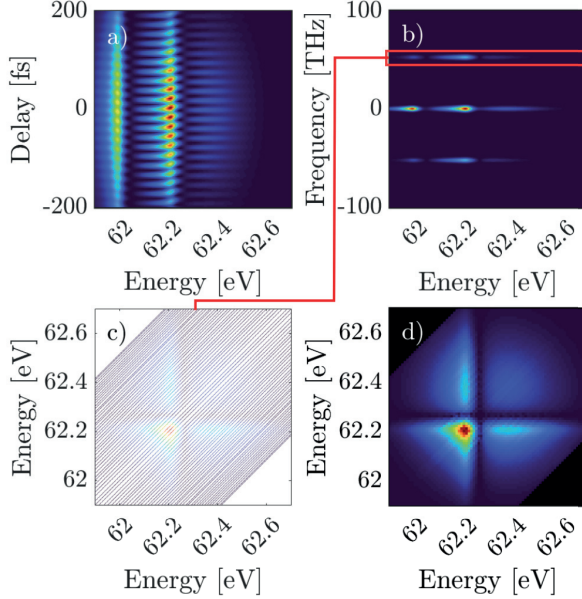


Figure 4.2: Reconstruction procedure of the KRAKEN protocol illustrated with simulations in He close to the $2s2p$ resonance. a) A pump-probe delay scan is measured with the femtosecond XUV pump and bichromatic IR probe. b) Fourier map obtained from Fourier transforming the spectrogram in a) along the delay axis for each energy bin. By selecting the component oscillating at frequency $\delta\omega$, a subdiagonal of the density matrix is retrieved. c) Repeating the procedure in a) and b) for a sequence of probe spectral components the sparse density matrix can be reconstructed. d) Continuous variable density matrix obtained by interpolating the sparse density matrix with a moving average. Figure adapted from paper VI.

4.3 Electron purity and bipartite entanglement

In general, when a short XUV pulse ionizes an atom, the final state can be written as,

$$|\psi_{\text{atom}}\rangle = \sum_j \int d\epsilon \, c_j(\epsilon) |j, \epsilon\rangle, \quad (4.3)$$

assuming a single angular momentum continuum channel, where j are the quantum numbers for the ion, and ϵ the scattering states describing the photoelectron wavepacket. The density matrix of the atom, assuming a pure state, is given by,

$$\hat{\rho}_{\text{atom}} = |\psi_{\text{atom}}\rangle \langle \psi_{\text{atom}}|. \quad (4.4)$$

However in photoelectron spectroscopy, only the photoelectron is measured and the observer does not know the quantum state of the ion. In quantum mechanics this loss of information has to be taken into account to properly describe the subsystem, by taking the trace over the degrees of freedom that are not measured. Therefore in our situation we have to trace over the ionic degrees of freedom. The density matrix of the photoelectron then becomes,

$$\begin{aligned} \hat{\rho}_{\text{electron}} &= \text{tr}_{\text{ion}}(\hat{\rho}_{\text{atom}}) = \\ &= \sum_j \int d\epsilon_1 d\epsilon_2 \, c_j^*(\epsilon_1) c_j(\epsilon_2) |\epsilon_1\rangle \langle \epsilon_2| \end{aligned} \quad (4.5)$$

If the ion and electron degrees of freedom are separable, i.e. if the coefficients factorize $c_j(\epsilon) = a_j b(\epsilon)$, the electron is a pure state, otherwise it is mixed.

The purity is often used to quantify the degree of coherence of a density matrix. The purity is defined as,

$$\gamma = \text{tr}(\hat{\rho}^2), \quad (4.6)$$

where the trace is the integral over the elements of the density matrix,

$$\gamma = \int d\epsilon \langle \epsilon | \hat{\rho}^2 | \epsilon \rangle \quad (4.7)$$

By inserting the completeness relation of the scattering states the purity can be expressed as [18],

$$\gamma = \int d\epsilon d\epsilon' \, |\rho(\epsilon, \epsilon')|^2 \quad (4.8)$$

What is notable about this expression is that the purity is not a function of the phase of the density matrix. The purity is a scalar value in the range $[1/d, 1]$, where d is the dimension of the Hilbert space. Since the Hilbert space of the scattering states is infinite dimensional, the purity of the maximally mixed state is 0.

4.3.1 Ion-photoelectron entanglement in neon and argon

In the case of argon and neon, the ionization threshold is split due to spin-orbit interaction. In paper **VI** we show that the state of the total system, assuming fully coherent XUV radiation, can be written as,

$$|\psi_{\text{atom}}\rangle = a_{1/2} |1/2\rangle \otimes \int d\epsilon b_{1/2}(\epsilon) |\epsilon\rangle + a_{3/2} |3/2\rangle \otimes \int d\epsilon b_{3/2}(\epsilon) |\epsilon\rangle, \quad (4.9)$$

where, $|j\rangle$, is the quantum state of the ion and $\int d\epsilon b_j(\epsilon) |\epsilon\rangle$, the quantum state of the photoelectron associated to a specific ionic state. $b_{3/2}(\epsilon)$ is identical to $b_{1/2}(\epsilon)$ up to a shift in energy corresponding to the spin-orbit splitting, ϵ_{SO} , $b_{3/2}(\epsilon) = b_{1/2}(\epsilon - \epsilon_{\text{SO}})$. The density matrix of the photoelectron is then,

$$\begin{aligned} \rho_{\text{electron}} &= p_{1/2} \int d\epsilon_1 d\epsilon_2 b_{1/2}(\epsilon_1) b_{1/2}^*(\epsilon_2) |\epsilon_1\rangle \langle \epsilon_2| \\ &\quad + p_{3/2} \int d\epsilon_1 d\epsilon_2 b_{1/2}(\epsilon_1 - \epsilon_{\text{SO}}) b_{1/2}^*(\epsilon_2 - \epsilon_{\text{SO}}) |\epsilon_1\rangle \langle \epsilon_2| \\ &= p_{1/2} \rho_{1/2} + p_{3/2} \rho_{3/2}, \end{aligned} \quad (4.10)$$

where $p_j = |a_j|^2$. The purity in the case of spin-orbit splitting is then given as,

$$\gamma = \text{tr}(\rho_{\text{electron}}^2) = p_{1/2}^2 + p_{3/2}^2 + 2p_{1/2}p_{3/2}\text{tr}(\rho_{1/2}\rho_{3/2}). \quad (4.11)$$

The last term is the trace over the product of the density matrices of the two spin-orbit components and can be represented as an overlap integral. The purity can be rewritten as,

$$\gamma = p_{1/2}^2 + p_{3/2}^2 + 2p_{1/2}p_{3/2} \left| \int d\epsilon b_{1/2}^*(\epsilon) b_{1/2}(\epsilon - \epsilon_{\text{SO}}) \right|^2. \quad (4.12)$$

For argon and neon the probabilities, $p_{1/2}$ and $p_{3/2}$, are given from the sum-rule, and p_j is proportional to the degeneracy. Therefore, using $p_{1/2} = 1/3$ and $p_{3/2} = 2/3$, gives,

$$\gamma = \frac{5}{9} + \frac{4}{9} \left| \int d\epsilon b_{1/2}^*(\epsilon) b_{1/2}(\epsilon - \epsilon_{\text{SO}}) \right|^2. \quad (4.13)$$

By changing the overlap integral, the purity of the photoelectron can be controlled. If the XUV bandwidth is much narrower than the spin-orbit splitting energy, $\sigma_{\text{XUV}} \ll \epsilon_{\text{SO}}$, the overlap integral is approximately zero and the purity is 5/9. This corresponds to the maximally mixed state of the photoelec-

tron. Instead, if the XUV bandwidth is much larger than the spin-orbit energy $\sigma_{\text{XUV}} \gg \epsilon_{\text{SO}}$ the overlap integral is approximately 1 giving a purity of 1 corresponding to a pure state. Since this is a bipartite state, electron + ion, assuming that the XUV is fully coherent, a reduced purity of the photoelectron implies entanglement between the photoelectron and the ion. The concurrence is an entanglement measure and can for bipartite states be written as [73],

$$\mathcal{C} = \sqrt{2(1 - \gamma)}. \quad (4.14)$$

A concurrence equal to one corresponds to a maximally entangled state and a concurrence of zero corresponds to a separable state. By changing the XUV bandwidth the overlap between the spin-orbit components can be controlled, and consequently the purity of the photoelectron and the ion-photoelectron entanglement.

4.4 Numerical simulations close to Fano resonances

In paper **VI**, we present the KRAKEN protocol and validate the protocol using simulations based on a model assuming finite pulses [64]. KRAKEN spectrograms are simulated from which the density matrix can be reconstructed, sub-diagonal by subdiagonal. The sparse density matrix is then interpolated using a moving average filter to give the continuous variable density matrix.

Figure 4.3 presents the amplitude and phase of the density matrix of a photoelectron wavepacket close to the $2s2p$ Fano resonance in helium, and the $3s^{-1}4p$ Fano resonance in argon. There is excellent agreement between the direct calculation and the numerical reconstruction using KRAKEN. The dark crosses in the amplitudes of the density matrices in helium and argon are due to the destructive interference of the Fano resonance. In argon, due to the spin-orbit splitting, the pattern repeats itself, resulting in two crosses. At the position of the destructive interference there is a phase jump due to the Fano resonance. Both the reconstructed amplitude and phase of the density matrix agree well with the direct calculation.

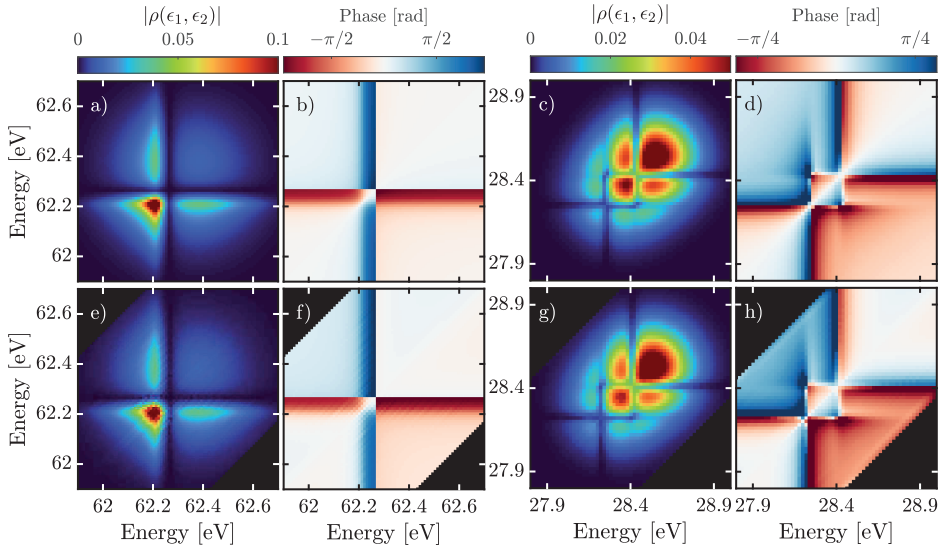


Figure 4.3: Amplitude and phase of density matrix of the $2s2p$ Fano resonance in helium from direct calculation (a,b) and using KRAKEN (e,f). Amplitude and phase of density matrix of the $3s^{-1}4p$ Fano resonance in argon from direct calculation (c,d) and using KRAKEN (g,h). Figure adapted from paper VI.

In Fig. 4.4 the purity and concurrence for the $3s^{-1}4p$ Fano resonance in argon is plotted against XUV bandwidth. For XUV bandwidth below 0.1 eV the purity is constant, since the two spin-orbit components do not overlap and the overlap integral is zero. In this region the state of the EWP is the maximally mixed state with a purity, $\gamma = 5/9$. As the bandwidth is increased, the overlap increases and the purity therefore increases. Conversely, the entanglement decreases for increasing XUV bandwidth. There is maximal entanglement between the electron and ion for XUV bandwidths less than 0.1 eV. There is excellent agreement between the purity and concurrence values reconstructed using KRAKEN (crosses) and the direct one-photon calculation (solid lines).

An intuitive interpretation of why the entanglement decreases when the overlap between the spin-orbit components increases is as follows. If the bandwidth is small enough so that there is no spectral overlap, by measuring the kinetic energy of the electron, we determine with certainty the state of the ion. However, if the XUV bandwidth is large enough, the spectral components associated to the ionic states $j = 1/2$ and $j = 3/2$ overlap. In this case, if we measure an electron with a kinetic energy in the range where the two components overlap, we do not know what is the state of the ion and the ionic wavefunction does not collapse.

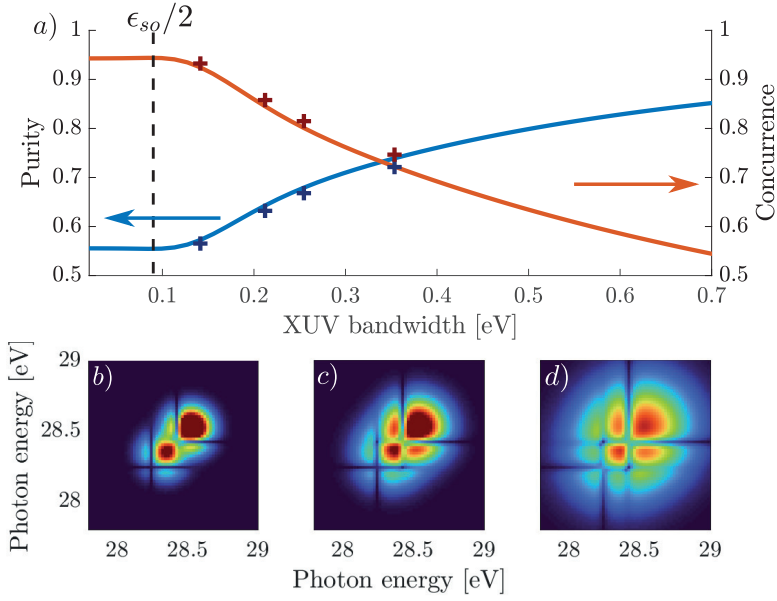


Figure 4.4: a) Purity (blue curve) and concurrence (red curve) vs. XUV bandwidth in argon calculated using a direct (1-photon) calculation. The dashed line indicates half the spin-orbit splitting energy in argon. For smaller bandwidths there is very little overlap between the spin-orbit components giving a purity of $5/9$. The crosses are the purity and concurrence values reconstructed using KRAKEN. Amplitude of density matrices in argon for bandwidths 0.14 b), 0.21 c), and 0.35 d) eV. The dark crosses in the density matrices is due to the destructive interference from the Fano resonances. Figure adapted from paper VI.

4.5 Experimental setup

KRAKEN measurements are very challenging and set high requirements on the experimental setup. A typical KRAKEN scan takes 8 hours to acquire, during which it is necessary for the pump-probe delay and laser intensity to be stable. Additionally the probe spectrum is required to be bichromatic with tunable spectral components. The spectral filtering of the probe decreases the probe peak intensity by two orders of magnitude, due to the increase of the probe pulse duration and the removal of most of the spectral components, making it challenging to have high enough intensity to allow two-photon transitions.

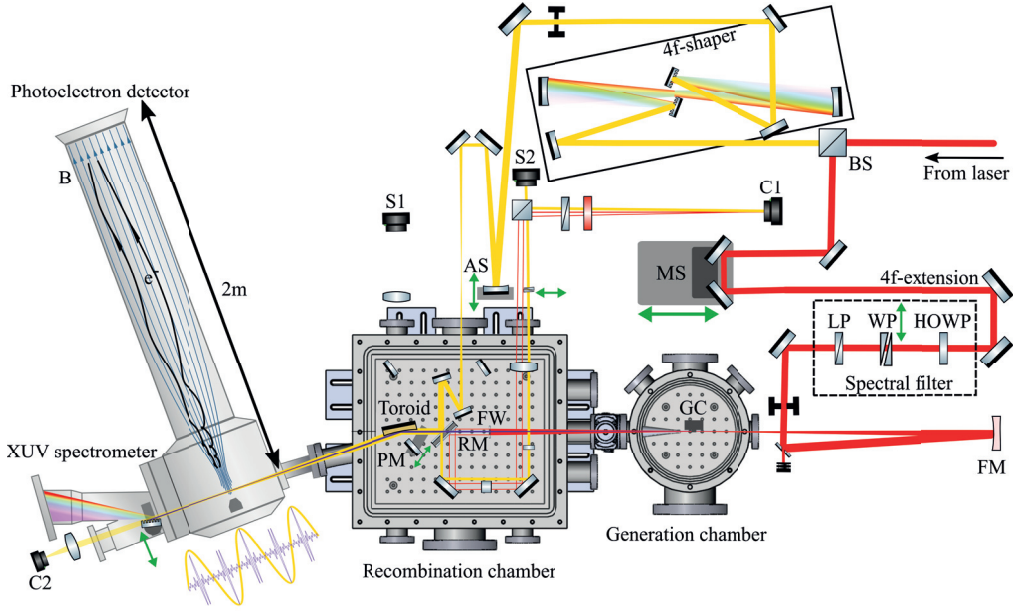


Figure 4.5: Schematic of the KRAKEN experimental setup. A folding mirror on a flip-mount has been flipped out of the beam path of the probe, sending the probe into the 4f-shaper. In the pump, the beam path is extended to compensate for the extension in the probe. The pump includes a spectral filter which enables independent central wavelengths of the pump and the probe. Figure adapted from paper VII.

Fig. 4.5 shows the experimental setup used for KRAKEN measurements. Most of the setup has been described in the previous chapter. Here we outline the specificities of these measurements (see also paper VII). A 4f-shaper is inserted in the probe of the Mach-Zehnder interferometer. The 4f-pulse shaper consists of three operations, an optical Fourier transform, spatial filtering in the Fourier plane, using slits, and inverse optical Fourier transform. The incident probe beam is sent on a reflection diffraction grating (1200 lines/mm, supplied from Spectrogon), that diffracts the beam. The diffracted beam is focused with a spherical mirror (focal length of 50 cm) on a line. In the Fourier plane, two slits, 3 mm wide, are placed. One slit is mounted on a motorized translation stage from Thorlabs and the other one is kept stationary. The entire slit configuration is mounted upside down above the gratings on a secondary translation stage for alignment purposes. After the Fourier plane the reverse process occurs, the pulse are focused with a 50 cm spherical mirror on an identical reflection diffraction

grating, resulting in a collimated beam after the 4f-shaper. To compensate for the longer beam path in the probe, there is a beam path extension in the pump such that after recombination of the pump and probe pulses there is temporal overlap. In the path extension of the pump, there is a tunable spectral filter that allows for tuning of the pump central wavelength independently from the probe.

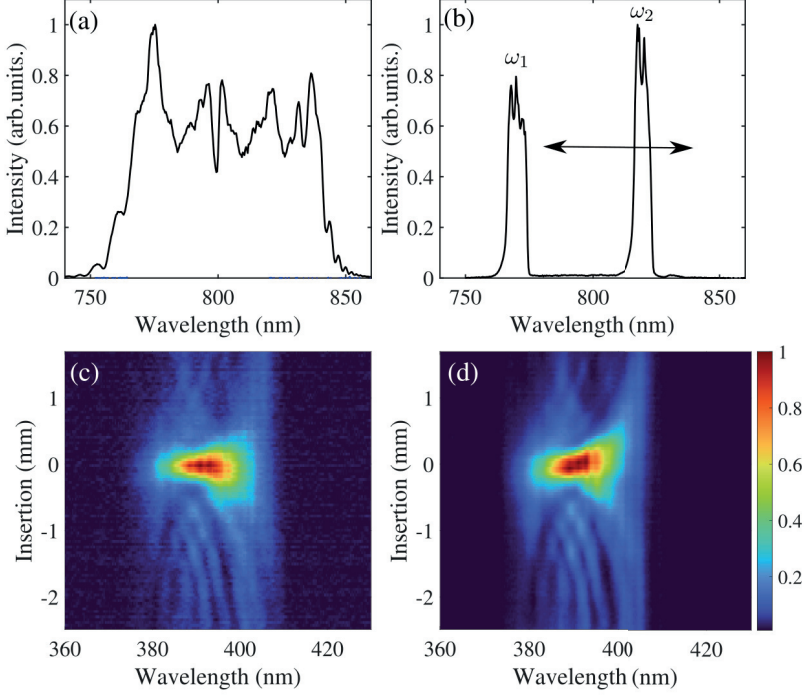


Figure 4.6: (a) Spectrum of the laser pulse. (b) Spectrum after passing through the 4f-shaper with two slits in the Fourier plane. Measured d-scan trace, before (c) and after (d) passing through the 4f-shaper, with no slits inserted. Figure adapted from paper VII.

In Fig. 4.6 the laser spectra are shown before (a) in black and after (b) passing through the 4f-shaper. By changing the slit position, the spectral content of the probe is controlled. In Fig. 4.6(c,d) dispersion scan (d-scan) [74, 75] measurements are shown before (c) and after (d) passing through the 4f-shaper, showing that the pulse is compressed after the pulse shaper. The probe spectra are recorded during a KRAKEN scan, and are later used for subdiagonal renormalization

according to the formula,

$$\rho_{\text{NORM}}(\epsilon, \epsilon + \delta\omega) = \frac{\rho_{\text{RAW}}(\epsilon, \epsilon + \delta\omega)}{I_{\text{XUV}} \sqrt{q_{\text{IR1}}(\omega_1) I_{\text{IR1}}(\omega_1) q_{\text{IR2}}(\omega_2) I_{\text{IR2}}(\omega_2)}}, \quad (4.15)$$

where I_{IR1} is the intensity of the first probe pulse (with frequency ω_1), I_{IR2} is the intensity of the second probe pulse (frequency ω_2), I_{XUV} is the harmonic intensity, q_{IR1} and q_{IR2} are the relative spectrometer responses at the two frequencies. I_{IR1} , I_{IR2} and I_{XUV} are integrated over their respective spectral peaks.

4.6 Experimental results

In paper **VIII**, we experimentally demonstrate the KRAKEN protocol by measuring the non-resonant continuous variable density matrix of photoelectrons created in helium, neon and argon by absorption of the 19th harmonic.

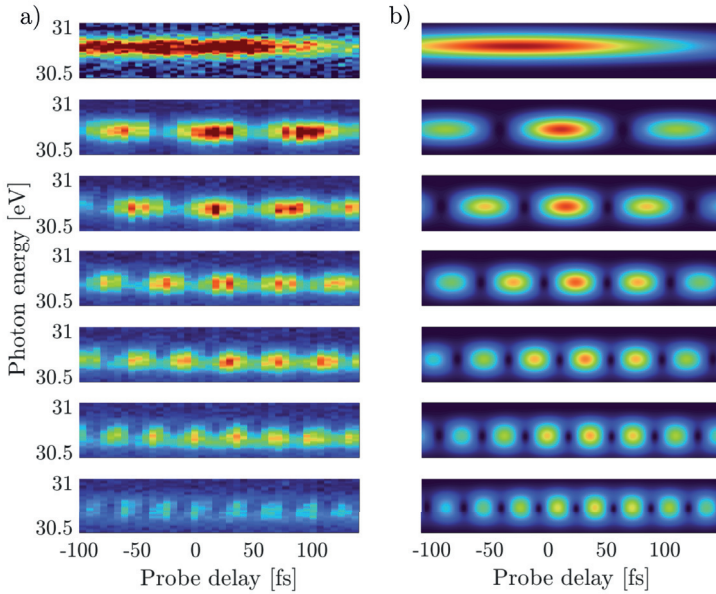


Figure 4.7: a) KRAKEN scans in helium for $\lambda_1 = 770$ nm, and $\lambda_2 = 770, 790, 800, 810, 820, 830, 840$ nm. b) Simulated KRAKEN scan in helium for $\lambda_1 = 770$ nm, and $\lambda_2 = 770, 790, 800, 810, 820, 830, 840$ nm. The XUV bandwidth is 0.14 eV (FWHM intensity) and the IR bandwidth 8 nm. Figure adapted from paper **VIII**.

Fig. 4.7 a) shows non-resonant KRAKEN scans in helium with increasing bi-chromatic probe wavelength separation. One spectral component is kept stationary at 770 nm, while the other spectral component is scanned between 790 and 840 nm in steps of 10 nm. When the wavelength difference is increased, the frequency of the sideband oscillations increases accordingly. A combination of germanium and aluminum filters are used in the pump arm to filter out the XUV radiation above H_{19} . Fig. 4.7 b) shows simulated KRAKEN scans in helium using a finite-pulse code based on the model by [64], showing excellent agreement with the measured KRAKEN scan.

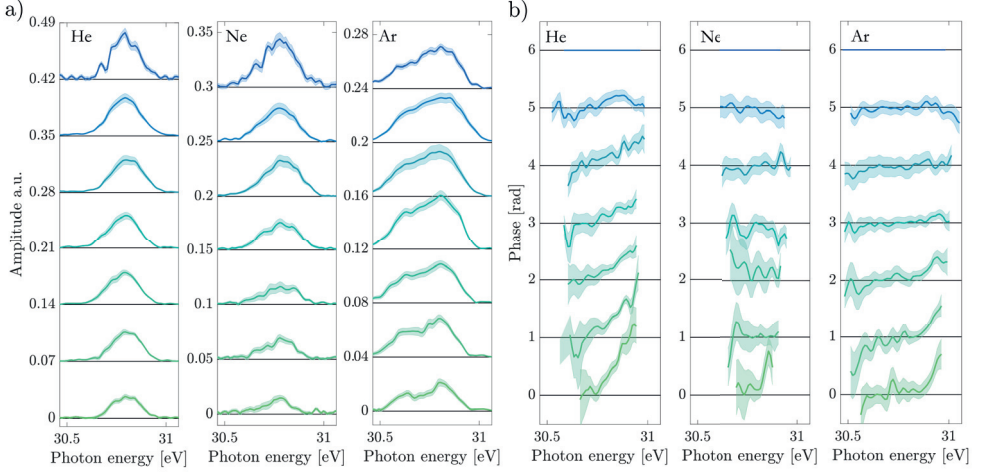


Figure 4.8: a) Amplitude of sideband oscillation for helium, neon and argon. Increasing frequency difference, $\delta\omega$, from blue to green. b) Phase of oscillation in helium, neon and argon. The phase curves are separated by 1 rad for visibility. Figure adapted from paper VIII.

By performing a cosine fit with a Gaussian envelope, for each energy bin, the amplitude and phase of the sideband oscillations are retrieved. Fig. 4.8 presents the measured amplitude a) and phase b) for helium, neon and argon. For increasing $\delta\omega$ the amplitude decreases. For the sideband phases, the spectral chirp increases in helium and argon while being constant in neon. The linear chirp comes from the femtosecond chirp, due to the intensity dependence of the accumulated phase in the continuum (see chapter 2). This explain the phases measured in helium and argon but it is unclear why the phase does not vary much in neon. We note nonetheless, as shown in Eq. (4.8), that the phase of the density matrix does not impact the calculation of the purity.

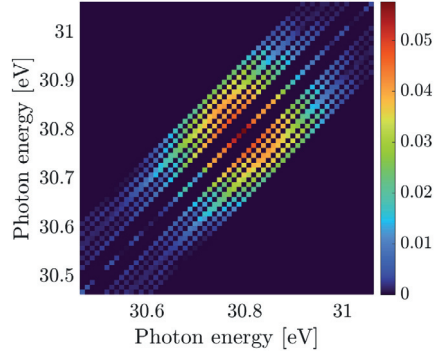


Figure 4.9: Sparse density matrix in helium reconstructed from the oscillation amplitudes.

Using the measured amplitudes it is possible to reconstruct the sparse density matrix as shown in Fig. 4.9. The subdiagonals in the reconstructed density matrix are placed according to Eq. (4.2).

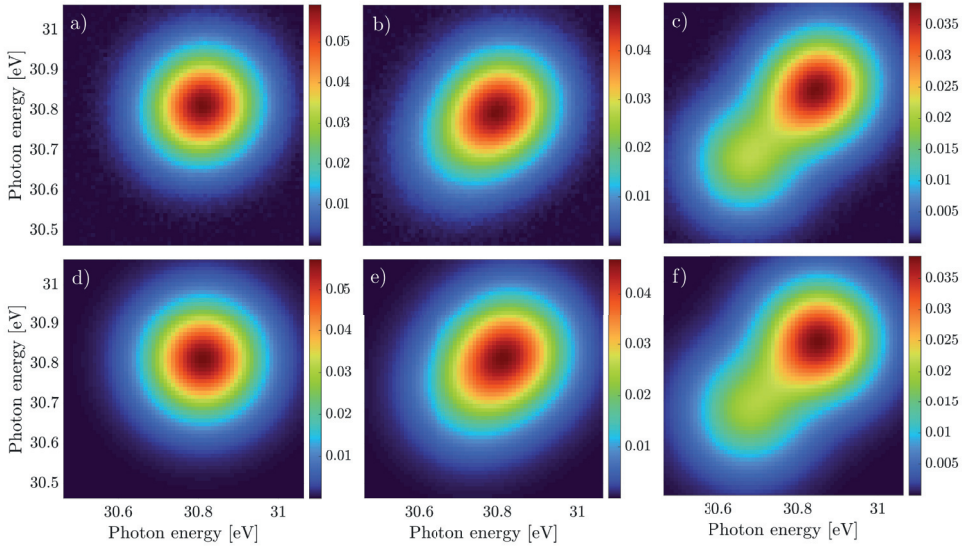


Figure 4.10: Reconstructed density matrices in helium a), neon b) and argon c) using KRAKEN. Density matrices from RPAE calculations in helium d), neon e) and argon f).

In order to retrieve the complete density matrix based on the sparse measurements the sparse density matrix is fitted using a Bayesian optimization algorithm based on Hamiltonian Monte Carlo methods. A numerical deconvolution pro-

cedure to compensate for the point spread function of the MBES is also applied. In Fig. 4.10 (a,b,c) the fitted and deconvolved density matrices are shown for helium, neon and argon and in Fig. 4.10 (c,d,e) the density matrices calculated using RRP AE are shown, showing a good agreement with the retrieved density matrices. From the continuous variable density matrices it is possible to calculate the purity.

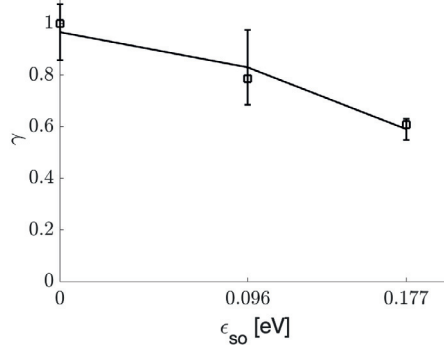


Figure 4.11: Reconstructed purity in helium ($\epsilon_{\text{SO}} = 0$), neon ($\epsilon_{\text{SO}} = 96$ meV) and argon ($\epsilon_{\text{SO}} = 177$ meV) using a XUV bandwidth of 0.14 eV (black error bars). Purity in helium, neon and argon from RRP AE calculations (black boxes).

In Fig. 4.11 the electron purity in helium, neon and argon for a XUV bandwidth of 0.14 eV is shown. In helium there is no spin-orbit splitting and the density matrix is a pure state, in neon the spin-orbit splitting energy is $\epsilon_{\text{SO}} = 96$ meV, and in argon the spin-orbit splitting energy is $\epsilon_{\text{SO}} = 177$ meV. For larger spin orbit splitting the overlap between the spin-orbit components is less, therefore the purity is reduced. The black boxes are the purity values from RRP AE calculations. The reduced purity of the photoelectron, in the case of neon and argon, implies entanglement between the ion and the photoelectron.

Through these measurements we validate the KRAKEN protocol experimentally by reconstructing the density matrix of photoelectrons emitted from helium, neon and argon atoms. This opens the possibility, using KRAKEN, to study the coherence of electron wavepackets in more complex systems.

Chapter 5

Summary and outlook

5.1 Summary

In this thesis, the photoelectron interferometry techniques, RABBIT and KRAKEN, are used to measure the wavefunctions and density matrices of electrons ionized by XUV light pulses. Using RABBIT measurements, broadband resonances, induced by electron correlation is studied with a train of attosecond XUV pulses and resonant photoionization is investigated using two consecutive harmonics, one of them close to the resonance. KRAKEN measurements are performed in helium, neon and argon from which the photoelectron density matrix is determined.

In papers **I** and **II**, broadband RABBIT measurements (Fig. 5.1 a)) are used to study electron correlation through the measurement of photoionization time-delays. In paper **I**, the photoionization time-delay differences between the $3s$ and $3p$ shell are measured across the $3s$ and $3p$ Cooper minima in argon. Theory and experiment agree well over a large spectral region except at the $3s$ Cooper minimum. A tentative explanation for the discrepancy is the influence of shake-up processes. In paper **II** ionization of xenon in the $4d$ -shell is studied in the region of the “giant dipole resonance”.

In papers **III**, **IV** and **V** energy-resolved RABBIT measurements (Fig. 5.1 b)) are performed to study resonant photoionization. In paper **III**, resonances via the $1s3p$, $1s4p$ and $1s5p$ states below threshold are investigated. In the case of the $1s4p$ resonance, the amplitude and phase of the electron wavepacket is measured as function of photoelectron kinetic energy and emission angle, showing phase jumps due to the resonance. These phase jumps are explained

using theoretical calculations based on perturbation theory. In paper **IV**, the spectral amplitude and phase of the photoelectron is measured across the $3s^{-1}4p$ Fano resonance in argon. Due to the high spectral resolution, we measure in some cases a close to 2π phase jump consistent with a complex valued Fano parameter, q . In paper **V**, resonant photoionization is studied using RABBIT in the vicinity of the $2s2p$ Fano resonance in helium. From the measurement of the spectral amplitude and phase, the Wigner function and density matrix of the photoelectron is reconstructed.

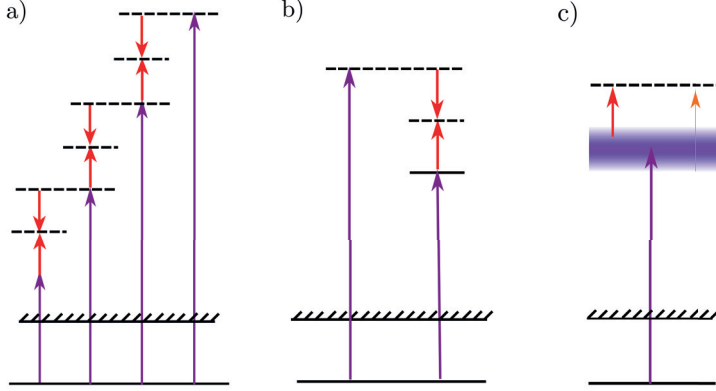


Figure 5.1: Energy diagrams for the measurement schemes used in this thesis. a) Energy diagram for broadband RABBIT used in the measurements of paper **I** and **II**. b) Energy diagram for narrowband energy resolved RABBIT used in the measurements of paper **III**, **IV** and **V**. c) Energy diagram for the KRAKEN protocol used in the numerical simulations of paper **VI** and in the measurements of paper **VIII**.

In paper **VI** the KRAKEN protocol is presented (Fig. 5.1 c)) and validated using numerical simulations performed in helium in the vicinity of the $2s2p$ Fano resonance and in argon close to the $3s^{-1}4p$ Fano resonance. We also show how KRAKEN can be used to probe bipartite entanglement between the ion and the photoelectron. In paper **VII** a new photoelectron interferometer for RABBIT and KRAKEN measurements is presented. The interferometer has high spectral resolution (< 50 meV), low temporal jitter (13 as) and is versatile in the sense that the central wavelength of the pump and probe field can be tuned independently. In paper **VIII** we present the first KRAKEN measurements. We reconstruct the density matrix in helium, neon and argon. In the case of neon and argon, we measure a purity less than one, implying entanglement between the ion and the photoelectron.

A central point in this thesis is the emphasis on high spectral resolution. The high spectral resolution enables the measurement of the close to 2π phase vari-

ation in paper **IV** as well as the quantum state reconstruction in paper **V**. The high spectral resolution is also critical for the KRAKEN measurements, as the spectrometer response is the main contribution to the experimental decoherence, as shown in paper **VI**.

5.2 Outlook

In this thesis, a transition has been made from the measurement of phase and time delays in atomic systems (RABBIT) to that of density matrices (KRAKEN). Naturally, this outlook will focus on how to apply, improve and extend KRAKEN measurements.

Having demonstrated the KRAKEN protocol experimentally, a natural next step is to perform KRAKEN measurements in more complex systems. For example, in simple molecules such as H_2 , where vibrational and electronic degrees of freedom are entangled. Another possible system of investigation is Auger decay. Auger decay is a three body problem with a slow electron, a fast electron and the ion. From KRAKEN measurements both the density matrix of the fast and the slow electron can be reconstructed. It may then be possible to characterize tripartite entanglement. Additionally, using KRAKEN on solid samples it may be possible to study the degree of coherence of electronic processes in solids.

Currently, a KRAKEN scan takes 8 hours to perform. This makes KRAKEN an extremely challenging experimental protocol, since the laser and the interferometer need to be stable for the total duration of the scan. In KRAKEN, a delay scan is recorded for each pair of probe spectral components. However, it is possible to parallelize this process and read out several subdiagonals simultaneously using a well chosen probe spectrum, including more than two spectral components. KRAKEN variants are currently being investigated both numerically and experimentally with the purpose of only needing a single delay scan to reconstruct the full density matrix. This would speed up the reconstruction time with an order of magnitude, opening up the possibility to perform several KRAKEN scans for different prepared states, opening the door to Quantum Process Tomography (QPT) of photoelectrons.

The KRAKEN protocol is a generalization of RABBIT that enables the determination of the degree of coherence of femtosecond electron pulses through the measurement of the photoelectron density matrix. The density matrix reconstructed using KRAKEN is measured at $t \rightarrow \infty$. It would be interesting to reconstruct the build-up [10] of the density matrix. Given the evolution

of the density matrix, the evolution of the purity can be retrieved, which in some systems could give insight into entanglement dynamics on the femtosecond timescale.

Author Contributions

Paper I: Attosecond photoionization dynamics in the vicinity of the Cooper minima in argon

In this paper, we measure photoionization time-delays between the $3s$ and $3p$ subshells of argon using Rainbow RABBIT across the $3s$ and $3p$ Cooper minima. The rapid variation of the time-delay differences across the $3p$ Cooper minima are reproduced with theoretical calculations using the Two-Photon Two-Color Random Phase Approximation with Exchange except in the region of the $3s$ Cooper minimum.

I participated with data analysis and signal processing of the results obtained in Lund, extracting the phases through a cosine fit and categorizing the relative amplitudes as well as interpretation of the data. I participated to the manuscript with comments and feedback.

Paper II: Attosecond electron–spin dynamics in xe 4d photoionization

In this paper, we studied photoionization time-delays in xenon in the 70-100 eV range by combining attosecond interferometry with coincidence spectroscopy. Supported by calculations using the relativistic random phase approximation, we identify two interfering ionization processes, the giant dipole resonance due to collective effects in $4d \rightarrow \epsilon f$ excitation with a fast decay time of a few tens of attoseconds and a narrow resonance at threshold induced by spin-flip transitions, with much longer decay time of several hundreds attoseconds. Our results provide new insight into the complex electron-spin dynamics of photo-induced phenomena.

I participated in taking the measurements and in the interpretation of the res-

ults. I also participated to the manuscript with comments and feedback.

Paper III: Resonant two-photon ionization of helium atoms studied by attosecond interferometry

In this paper, we study resonant two-photon ionization of helium via the $1s3p$, $1s4p$ and $1s5p$ states using angle resolved Rainbow RABBIT. We measure phase jumps across the $1s4p$ state in energy and emission angle that we then interpret using perturbation theory.

I participated in taking the measurements and in the data analysis. I also participated to the manuscript with comments and feedback.

Paper IV: Breaking the time symmetry of Fano resonances in attosecond photoelectron interferometry

In this paper, we study the $3s^{-1}4p$ Fano resonance in argon using Rainbow RABBIT and measure a larger than π phase variation across the resonance in SB 16. This huge phase variation is enabled by a complex q -parameter with origin from the interaction of the bound state with the IR probe.

I participated in taking the measurements, in data analysis, and in the writing of the manuscript.

Paper V: Probing electronic decoherence with high-resolution attosecond photoelectron interferometry

In this paper, we study the $2s2p$ Fano resonance in helium using Rainbow Rabbit measurements. From the amplitude and phase of the electron wavepacket we are able to quantify the purity of the EWP and identify the dominant decoherence channel. We also calculate the evolution of the purity.

I participated to the data analysis, and more specifically to the deconvolution of the data, and to the interpretation of the results. I also participated to the manuscript with comments and feedback.

Paper VI: Continuous-variable quantum state tomography of photoelectrons

In this paper, we propose the KRAKEN method, a continuous variable quantum state tomography protocol for continuum states using attosecond pump probe spectroscopy. Additionally a method to control ion-photoelectron entanglement is presented.

I took a large part in the derivation of the method. I performed simulations that verify the method. I also participated in writing of the manuscript.

Paper VII: Ultra-stable and versatile high-energy resolution setup for attosecond photoelectron spectroscopy

In this paper, we present and characterize a new attosecond photoelectron interferometer. We show a low temporal jitter of 13 as when actively stabilizing the delay, as well as a high tunability. One objective of the upgrade of the setup was to enable the experimental realization of the KRAKEN protocol.

I participated in the design and implementation of the new inteferometer. I also participated to the manuscript with comments and feedback.

Paper VIII: Measuring the quantum state of a photoelectron

In this paper, we present the first KRAKEN measurements. We characterize the denisty matrix of the photoelecron in helium, neon and argon, and quantify the degree of coherence of the photoelectron.

I participated in the experiment design and the building of the experimental setup. I took a large part in the measurements, the data analysis, the interpretation of the results and the writing of the manuscript.

Acknowledgments

I have enjoyed being a PhD student. I think there are very few workplaces that give you such freedom when starting in a new organization. The type of research performed in this thesis is based on teamwork, so there are many people I would like to thank for contributing to my thesis and for making my PhD studies interesting and fun.

First, I would like to thank my main supervisor Anne L’Huillier for hiring me as a PhD student and supporting me for these five years. Anne gave me freedom to explore research areas I found interesting, while with great intuition guiding me. I think you are a great inspiration as a leader. Secondly, I would like to thank my supervisors Cord Arnold and Mathieu Gisselbrecht. I have really enjoyed the discussions with the both of you.

I would like to thank the members of the group, David Busto, Lana Neoricic, Robin Weissenbilder, Mattias Ammitzböll, Sizuo Luo, Shiyang Zhong, Marcus Isinger and Saga Westerberg. Thank you David for teaching me about atto-second physics through my continuous stream of questions over the years. It has been great working creatively with you to solve hard problems. Thank you Robin for being the best office mate, Florida was great! Thank you Mattias for your positive energy and social personality, I enjoyed singing Hamilton karaoke with you while we aligned the 4f-shaper (not super succesfully). Thank you Lana for being kind and introducing me to the group. Finally, thank you Sizuo, It has been great getting to know you, without you I do not think the KRAKEN protocol would have been realized during my PhD. I hope I can come visit you and your family in Changchun.

I would like to thank all the collaborators of the projects I have been involved in. I would like to especially thank Daniel Finkelstein-Shapiro for your enthusiasm for the KRAKEN protocol and your ideas on how to formalize the protocol. Thank you Christoph Dittel for your insight and rigor, one of the best moments during my PhD was when you validated the KRAKEN derivation. Thank you

Leon Petersson for appearing with an excellent ab initio code for KRAKEN. Thank you Shahnawaz Ahmed for your contribution with the machine learning methods, it was great to work with you. Thank you Ron Demjaha, it was fun to discuss math and physics with you. Thank you Chen Guo, for your help with the fast Fourier transform and your help with the 4f-shaper. Thank you Richard Squibb and Raimund Feifel, for lending us the MBES. Additionally, thank you Raimund for coordinating the KAW grant, “Attosecond chronoscopy of electron wave-packets probing entanglement and time-ordering of quantum processes” that co-funded my PhD. Thank you Christina Alexandridi, Dominique Platzter, Lou Barreau, Margherita Turconi and Pascal Salières, for the nice collaboration. Thank you Per Eng-Johnson for lending the attolab the VMI for the VMI campaign. Thank you Jasper Peschel, Hampus Wikmark, Jan Lahl and Sylvain Maclot for the nice collaboration during the VMI campaign. Thank you Tõnu Pullerits and Andreas Buchleitner for all the input on the KRAKEN protocol. Additionally, thank you Saikat Nandi, David Kroon and Venus Poulain.

In this thesis I have collaborated with a few theorists that I would like to thank. Thank you Marcus Dahlström, Eva Lindroth, Jimmy Vindblad, Göran Wendin, Anton Ljungdahl, Fernando Martín, Luca Argenti, Carlos Marante, Roger Y. Bello Romero and Anton Frisk Kockum for the nice collaborations.

At the division of Atomic Physics there is a great atmosphere and there are many people I would like to thank for this. I would like to thank Neven Ibrakovic for helping me with the FRED labs, it was great teaching together with you. Thank you Emma Simpson for sharing my taste in pencils and calendars, and all the nice discussions. Thank you Samuel Bengtsson for all your help in the lab. Thank you Mattias Bertolino for the regular coffee breaks and physics discussions, it was great to have a friend from Uppsala as a colleague. Thank you Ivan Sytsevich and Alexander Permogorov for the Zakuski evenings among other things. I hope we can realize the trip in the future. Thank you Anders Persson for giving me advice about gratings, and lending me grating mounts. Thank you Claes-Göran Wahlström, Jörgen Larsson, Anne Petersson-Ljungbeck, Åke Johansson and Maria Algotsson for helping me with administration. A big thanks to the rest of you not written out explicitly, such a nice working environment is not something to take for granted.

I would like to thank Diskopunk for being the best friends, and Harald Forsmark for playing chess with me during corona. It is great to discuss the interface between philosophy and physics with you.

Finally I would like to thank my family, my wife Gjertrud Laurell, and my sons Tarjei and Skule.

References

- [1] H. E. Edgerton. *Flash! Seeing the Unseen by Ultra High-Speed Photography*. Charles T. Branford Company, Boston, MA, 1939.
- [2] A. McPherson, G. Gibson, H. Jara, U. Johann, T. S. Luk, I. A. McIntyre, K. Boyer, and C. K. Rhodes. Studies of multiphoton production of vacuum-ultraviolet radiation in the rare gases. *Journal of the Optical Society of America B*, 4:595–601, 1987.
- [3] M. Ferray, A. L’Huillier, X. Li, L. Lompre, G. Mainfray, and C. Manus. Multiple-harmonic conversion of 1064 nm radiation in rare gases. *Journal of Physics B: Atomic, Molecular and Optical Physics*, **21**:L31–L35, 1988.
- [4] P. M. Paul, E. S. Toma, P. Breger, G. Mullot, F. Augé, P. Balcou, H. G. Muller, and P. Agostini. Observation of a train of attosecond pulses from high harmonic generation. *Science*, 292(5522):1689–1692, 2001.
- [5] F. Krausz and M. Ivanov. Attosecond physics. *Review of Modern Physics*, 81(1):163–234, 2009.
- [6] K. Klünder, J. M. Dahlström, M. Gisselbrecht, T. Fordell, M. Swoboda, D. Guénot, P. Johnsson, J. Caillat, J. Mauritsson, A. Maquet, R. Taïeb, and A. L’Huillier. Probing single-photon ionization on the attosecond time scale. *Physical Review Letters*, 106:143002, 2011.
- [7] E. P. Månsson, D. Guénot, C. L. Arnold, D. Kroon, S. Kasper, J. M. Dahlström, E. Lindroth, A. S. Kheifets, A. L’Huillier, S. L. Sorensen, et al. Double ionization probed on the attosecond timescale. *Nature Phys.*, 10:207–211, 2014.
- [8] M. Kotur, D. Guénot, A. Jiménez-Galán, D. Kroon, E. W. Larsen, M. Louisy, S. Bengtsson, M. Miranda, J. Mauritsson, C. L. Arnold, S. E. Canton, M. Gisselbrecht, T. Carette, J. M. Dahlström, E. Lindroth,

- A. Maquet, L. Argenti, F. Martín, and A. L’Huillier. Spectral phase measurement of a Fano resonance using tunable attosecond pulses. *Nature Communications*, 7:10566–, 2016.
- [9] S. Heuser, Á. Jiménez Galán, C. Cirelli, C. Marante, M. Sabbar, R. Boge, M. Lucchini, L. Gallmann, I. Ivanov, A. S. Kheifets, J. M. Dahlström, E. Lindroth, L. Argenti, F. Martín, and U. Keller. Angular dependence of photoemission time delay in helium. *Physical Review A*, 94(6):063409–, 2016.
- [10] V. Gruson, L. Barreau, Á. Jiménez-Galan, F. Risoud, J. Caillat, A. Maquet, B. Carré, F. Lepetit, J.-F. Hergott, T. Ruchon, L. Argenti, R. Taïeb, F. Martín, and P. Salières. Attosecond dynamics through a fano resonance: Monitoring the birth of a photoelectron. *Science*, 354(6313):734–738, 2016.
- [11] I. Jordan, M. Huppert, S. Pabst, A. S. Kheifets, D. Baykusheva, and H. J. Wörner. Spin-orbit delays in photoemission. *Physical Review A*, 95(1):013404–, 2017.
- [12] S. Haessler, B. Fabre, J. Higuët, J. Caillat, T. Ruchon, P. Breger, B. Carré, E. Constant, A. Maquet, E. Mével, P. Salières, R. Taïeb, and Y. Mairesse. Phase-resolved attosecond near-threshold photoionization of molecular nitrogen. *Phys. Rev. A*, 80:011404, 2009.
- [13] S. Beaulieu, A. Comby, A. Clergerie, J. Caillat, D. Descamps, N. Dudovich, B. Fabre, R. Gêneaux, F. Légaré, S. Petit, B. Pons, G. Porat, T. Ruchon, R. Taïeb, V. Blanchet, and Y. Mairesse. Attosecond-resolved photoionization of chiral molecules. *Science*, 358(6368):1288–1294, 2017.
- [14] L. Cattaneo, J. Vos, R. Y. Bello, A. Palacios, S. Heuser, L. Pedrelli, M. Lucchini, C. Cirelli, F. Martín, and U. Keller. Attosecond coupled electron and nuclear dynamics in dissociative ionization of H_2 . *Nature Physics*, 14(7):733–738, 2018.
- [15] J. Vos, L. Cattaneo, S. Patchkovskii, T. Zimmermann, C. Cirelli, M. Lucchini, A. Kheifets, A. S. Landsman, and U. Keller. Orientation-dependent stereo wigner time delay and electron localization in a small molecule. *Science*, 360(6395):1326–1330, 2018.
- [16] R. Locher, L. Castiglioni, M. Lucchini, M. Greif, L. Gallmann, J. Osterwalder, M. Hengsberger, and U. Keller. Energy-dependent photoemission delays from noble metal surfaces by attosecond interferometry. *Optica*, 2(5):405–410, 2015.

- [17] L. Kasmi, M. Lucchini, L. Castiglioni, P. Kliuiev, J. Osterwalder, M. Hengsberger, L. Gallmann, P. Krüger, and U. Keller. Effective mass effect in attosecond electron transport. *Optica*, 4(12):1492–1497, 2017.
- [18] C. Bourassin-Bouchet, L. Barreau, V. Gruson, J.-F. Hergott, F. Quéré, P. Salières, and T. Ruchon. Quantifying decoherence in attosecond metrology. *Physical Review X*, 10(3):031048, 2020.
- [19] L.-M. Koll, L. Maikowski, L. Drescher, T. Witting, and M. J. J. Vrakking. Experimental control of quantum-mechanical entanglement in an attosecond pump-probe experiment. *Phys. Rev. Lett.*, 128:043201, 2022.
- [20] M. Lewenstein, M. F. Ciappina, E. Pisanty, J. Rivera-Dean, P. Stammer, T. Lamprou, and P. Tzallas. Generation of optical schrödinger cat states in intense laser–matter interactions. *Nature Physics*, 17(10):1104–1108, 2021.
- [21] K. E. Priebe, C. Rathje, S. V. Yalunin, T. Hohage, A. Feist, S. Schäfer, and C. Ropers. Attosecond electron pulse trains and quantum state reconstruction in ultrafast transmission electron microscopy. *Nature Photonics*, 11(12):793–797, 2017.
- [22] A. S. Maxwell, L. B. Madsen, and M. Lewenstein. Entanglement of orbital angular momentum in non-sequential double ionization. *Nature Communications*, 13(1):4706, 2022.
- [23] M. Y. Amus’ya, N. A. Cherepkov, and L. V. Chernysheva. Cross section for the photoionization of noble-gas atoms with allowance for multielectron correlations. 1971.
- [24] G. Wendin. Collective resonance in the 4d10 shell in atomic xe. *Physics Letters A*, 37(5):445–446, 1971.
- [25] E. Wigner. On the Quantum Correction For Thermodynamic Equilibrium. *Phys. Rev.*, **40**:749, 1932.
- [26] J. Ville. Théorie et applications de la notion de signal analytique. *Cables et transmission*, 2A:61-74, 1948.
- [27] F. A. F. Hlawatsch. *Time-Frequency Analysis*. Wiley-ISTE, 2013.
- [28] T. H. Maiman. Stimulated optical radiation in Ruby. *Nature*, **187**:493, 1960.
- [29] L. E. Hargrove, R. L. Fork, and M. A. Pollack. Locking of HeNe laser modes induced by synchronous intracavity modulation. *Applied Physics Letters*, 5(1):4–5, 1964.

- [30] X. H. Huang, J. M. Zuo, and J. C. Spence. Wavefront reconstruction for in-line holograms formed by pure amplitude objects. *Applied Surface Science*, 148:229–234, 1999.
- [31] G. A. Mourou, T. Tajima, and S. V. Bulanov. Optics in the relativistic regime. *Rev. Mod. Phys.*, 78:309–371, 2006.
- [32] D. Strickland and G. Mourou. Compression of amplified chirped optical pulses. *Opt. Commun.*, **56**:219, 1985.
- [33] K. J. Schafer, B. Yang, L. F. DiMauro, and K. C. Kulander. Above threshold ionization beyond the high harmonic cutoff. *Phys. Rev. Lett.*, **70**:1599, 1993.
- [34] P. Corkum. Plasma perspective on strong-field multiphoton ionization. *Phys. Rev. Lett.*, **71**:1994, 1993.
- [35] K. C. Kulander, K. J. Schafer, and J. L. Krause. Dynamics of short-pulse excitation, ionization and harmonic conversion. In *Super-Intense Laser-Atom Physics*. Plenum Press, New York, 1993.
- [36] M. Lewenstein, P. Balcou, M. Ivanov, A. L’Huillier, and P. Corkum. Theory of high-order harmonic generation by low-frequency laser fields. *Physical Review A*, 49:2117–2132, 1994.
- [37] D. Popmintchev, B. R. Galloway, M.-C. Chen, F. Dollar, C. A. Mancuso, A. Hankla, L. Miaja-Avila, G. O’Neil, J. M. Shaw, G. Fan, S. Ališauskas, G. Andriukaitis, T. Balčiunas, O. D. Mücke, A. Pugzlys, A. Baltuška, H. C. Kapteyn, T. Popmintchev, and M. M. Murnane. Near- and Extended-Edge X-Ray-Absorption Fine-Structure Spectroscopy Using Ultrafast Coherent High-Order Harmonic Supercontinua. *Physical Review Letters*, 120:093002, 2018.
- [38] A. S. Johnson, T. Avni, E. W. Larsen, D. R. Austin, and J. P. Marangos. Attosecond soft x-ray high harmonic generation. *Philosophical Transactions of the Royal Society A: Mathematical, Physical and Engineering Sciences*, 377(2145):20170468, 2019.
- [39] J. Tate, T. Augustine, H. G. Muller, P. Salieres, P. Agostini, and L. F. DiMauro. Scaling of Wave-Packet Dynamics in an Intense Midinfrared Field. *Phys. Rev. Lett.*, 98:013901, 2007.
- [40] M. Bellini, C. Lyngå, A. Tozzi, M. Gaarde, C. Delfin, T. Hänsch, A. L’Huillier, and C.-G. Wahlström. Temporal coherence of ultrashort high-order harmonic pulses. *Phys. Rev. Lett.*, 81:297, 1998.

- [41] M. B. Gaarde, J. L. Tate, and K. J. Schafer. Macroscopic aspects of attosecond pulse generation. *J. Phys. B*, 41:132001, 2008.
- [42] C. M. Heyl, C. L. Arnold, A. Couairon, and A. L’Huillier. Introduction to macroscopic power scaling principles for high-order harmonic generation. *J. Phys. B: At., Mol. Opt. Phys.*, 50(1):013001, 2017.
- [43] G. Farkas and C. Tóth. Proposal for attosecond light pulse generation using laser induced multiple-harmonic conversion processes in rare gases. *Phys. Lett. A*, **168**:447, 1992.
- [44] S. E. Harris, J. J. Macklin, and T. W. Hänsch. Atomic scale temporal structure inherent to high-order harmonic generation. *Opt. Commun.*, **100**:487, 1993.
- [45] A. Einstein. Über einen die Erzeugung und Verwandlung des Lichtes betreffenden heuristischen Gesichtspunkt. *Ann. Physik*, 322:132, 1905.
- [46] E. P. Wigner. Lower limit for the energy derivative of the scattering phase shift. *Phys. Rev.*, 98:145–147, 1955.
- [47] J. M. Dahlström, D. Guénot, K. Klünder, M. Gisselbrecht, J. Mauritsson, A. L’Huillier, A. Maquet, and R. Taïeb. Theory of attosecond delays in laser-assisted photoionization. *Chem. Phys.*, 414:53–64, 2013.
- [48] W. Pauli. General principles of quantum mechanics. *Springer-Verlag Berlin Heidelberg*, 1980.
- [49] U. Fano. Effects of configuration interaction on intensities and phase shifts. *Physical Review*, 124(6):1866, 1961.
- [50] C. Cirelli, C. Marante, S. Heuser, C. L. M. Petersson, Á. J. Galán, L. Argenti, S. Zhong, D. Busto, M. Isinger, S. Nandi, S. Maclot, L. Rading, P. Johnsson, M. Gisselbrecht, M. Lucchini, L. Gallmann, J. M. Dahlström, E. Lindroth, A. L’Huillier, F. Martín, and U. Keller. Anisotropic photoemission time delays close to a fano resonance. *Nature Communications*, 9(1):1–9, 2018.
- [51] M. Turconi, L. Barreau, D. Busto, M. Isinger, C. Alexandridi, A. Harth, R. J. Squibb, D. Kroon, C. L. Arnold, R. Feifel, M. Gisselbrecht, L. Argenti, F. Martín, A. L’Huillier, and P. Salières. Spin-orbit-resolved spectral phase measurements around a fano resonance. *Journal of Physics B: Atomic, Molecular and Optical Physics*, 53(18):184003, 2020.

- [52] D. Busto, L. Barreau, M. Isinger, M. Turconi, C. Alexandridi, A. Harth, S. Zhong, R. J. Squibb, D. Kroon, S. Plogmaker, M. Miranda, Á. Jiménez-Galán, L. Argenti, C. L. Arnold, R. Feifel, F. Martín, M. Gisselbrecht, A. L’Huillier, and P. Salières. Time–frequency representation of autoionization dynamics in helium. *Journal of Physics B: Atomic, Molecular and Optical Physics*, 51(4):044002, 2018.
- [53] L. Barreau, C. L. M. Petersson, M. Klinker, A. Camper, C. Marante, T. Gorman, D. Kiewewetter, L. Argenti, P. Agostini, J. González-Vázquez, P. Salières, L. F. DiMauro, and F. Martín. Disentangling spectral phases of interfering autoionizing states from attosecond interferometric measurements. *Physical Review Letters*, 122(25):253203.
- [54] A. Kaldun, A. Blättermann, V. Stooß, S. Donsa, H. Wei, R. Pazourek, S. Nagele, C. Ott, C. D. Lin, J. Burgdörfer, and T. Pfeifer. Observing the ultrafast buildup of a fano resonance in the time domain. *Science*, 354(6313):738–741, 2016.
- [55] C. Ott, A. Kaldun, P. Raith, K. Meyer, M. Laux, J. Evers, C. H. Keitel, C. H. Greene, and T. Pfeifer. Lorentz meets fano in spectral line shapes: A universal phase and its laser control. *Science*, 340(6133):716–720, 2013.
- [56] C. Ott, A. Kaldun, L. Argenti, P. Raith, K. Meyer, M. Laux, Y. Zhang, A. Blättermann, S. Hagstotz, T. Ding, et al. Reconstruction and control of a time-dependent two-electron wave packet. *Nature*, 516(7531):374–378, 2014.
- [57] W.-C. Chu and C. D. Lin. Photoabsorption of attosecond xuv light pulses by two strongly laser-coupled autoionizing states. *Phys. Rev. A*, 85(1):013409, 2012.
- [58] V. Vénierd, R. Taïeb, and A. Maquet. Two-Color Multiphoton Ionization of Atoms Using High-Order Harmonic Radiation. *Phys. Rev. Lett.*, 74:4161, 1995.
- [59] H. Muller. Reconstruction of attosecond harmonic beating by interference of two-photon transitions. *Appl. Phys. B*, 74:17, 2002.
- [60] V. Vénierd, R. Taïeb, and A. Maquet. Phase dependence of (N+1)-color (N>1) ir-uv photoionization of atoms with higher harmonics. *Phys. Rev. A*, 54:721, 1996.
- [61] C. Bourassin-Bouchet and M.-E. Couprie. Partially coherent ultrafast spectrography. *Nature Communications*, 6(1).

- [62] M. Schultze, M. Fieß, N. Karpowicz, J. Gagnon, M. Korbman, M. Hofstetter, S. Neppl, A. L. Cavalieri, Y. Komninos, T. Mercouris, C. A. Nicolaides, R. Pazourek, S. Nagele, J. Feist, J. Burgdörfer, A. M. Azzeer, R. Ernstorfer, R. Kienberger, U. Kleineberg, E. Goulielmakis, F. Krausz, and V. S. Yakovlev. Delay in photoemission. *Science*, 328:1658–1662, 2010.
- [63] M. Isinger, R. J. Squibb, D. Busto, S. Zhong, A. Harth, D. Kroon, S. Nandi, C. L. Arnold, M. Miranda, J. M. Dahlström, E. Lindroth, R. Feifel, M. Gisselbrecht, and A. L’Huillier. Photoionization in the time and frequency domain. *Science*, 358(6365):893–896, 2017.
- [64] Á. Jiménez-Galán, F. Martín, and L. Argenti. Two-photon finite-pulse model for resonant transitions in attosecond experiments. *Physical Review A*, 93(2):023429, 2016.
- [65] A. Autuori, D. Platzer, M. Lejman, G. Gallician, L. Maëder, A. Covolo, L. Bosse, M. Dalui, D. Bresteau, J.-F. Hergott, O. Tcherbakoff, H. J. B. Marroux, V. Lorient, F. Lépine, L. Poisson, R. Taïeb, J. Caillat, and P. Salières. Anisotropic dynamics of two-photon ionization: An attosecond movie of photoemission. *Science Advances*, 8(12):eabl7594, 2022.
- [66] D. Busto, H. Laurell, D. Finkelstein-Shapiro, C. Alexandridi, M. Isinger, S. Nandi, R. J. Squibb, M. Turconi, S. Zhong, C. L. Arnold, et al. Probing electronic decoherence with high-resolution attosecond photoelectron interferometry. *Eur. Phys. J. D*, 76:112, 2022.
- [67] W. H. Richardson. Bayesian-based iterative method of image restoration. *Journal of the Optical Society of America*, 62(1):55.
- [68] L. B. Lucy. An iterative technique for the rectification of observed distributions. *The Astronomical Journal*, 79:745.
- [69] M. Drescher, M. Hentschel, R. Kienberger, M. Uiberacker, V. Yakovlev, A. Scrinzi, T. Westerwalbesloh, U. Kleineberg, U. Heinzmann, and F. Krausz. Time-resolved atomic inner-shell spectroscopy. *Nature*, 419:803, 2002.
- [70] J. Yuen-Zhou, J. J. Krich, M. Mohseni, and A. Aspuru-Guzik. Quantum state and process tomography of energy transfer systems via ultrafast spectroscopy. *Proceedings of the National Academy of Sciences*, 108(43):17615–17620, 2011.
- [71] J. Yuen-Zhou, D. H. Arias, D. M. Eisele, C. P. Steiner, J. J. Krich, M. G. Bawendi, K. A. Nelson, and A. Aspuru-Guzik. Coherent exciton

- dynamics in supramolecular light-harvesting nanotubes revealed by ultrafast quantum process tomography. *ACS nano*, 8(6):5527–5534, 2014.
- [72] P. Hamm and M. Zanni. *Concepts and methods of 2D infrared spectroscopy*. Cambridge University Press, 2011.
- [73] F. Mintert, A. R. Carvalho, M. Kuś, and A. Buchleitner. Measures and dynamics of entangled states. *Physics Reports*, 415(4):207–259, 2005.
- [74] M. Miranda, T. Fordell, C. Arnold, A. L’Huillier, and H. Crespo. Simultaneous compression and characterization of ultrashort laser pulses using chirped mirrors and glass wedges. *Opt. Express*, 20(1):688–697, 2012.
- [75] M. Miranda, C. L. Arnold, T. Fordell, F. Silva, B. Alonso, R. Weigand, A. L’Huillier, and H. Crespo. Characterization of broadband few-cycle laser pulses with the d-scan technique. *Opt. Express*, 20(17):18732–18743, 2012.

